

EVOLUTION OF BIAS IN DIFFERENT COSMOLOGICAL MODELS

PEDRO COLÍN

Instituto de Astronomía, Universidad Nacional Autónoma de México, C.P. 04510, México, D.F., México

ANATOLY A. KLYPIN AND ANDREY V. KRAVTSOV

Astronomy Department, New Mexico State University, Box 30001, Department 4500, Las Cruces, NM 88003-0001

AND

ALEXEI M. KHOKHLOV

Laboratory for Computational Physics and Fluid Dynamics, Code 6404, Naval Research Laboratory, Washington, DC 20375

Received 1998 September 22; accepted 1999 May 6

ABSTRACT

We study the evolution of the halo-halo correlation function and small-scale ($\approx 0.2\text{--}7 h^{-1}$ Mpc) bias in four cosmological models (Λ CDM, OCDM, τ CDM, and SCDM) using very high resolution n -body simulations with a dynamical range of $\sim 10,000\text{--}32,000$ (force resolution of $\approx 2\text{--}4 h^{-1}$ kpc and particle mass of $\approx 10^9 h^{-1} M_\odot$). The high force and mass resolution allows dark matter halos to survive in the tidal fields of high-density regions and thus prevents the ambiguities related with the “overmerging problem.” This allows us to estimate for the first time the evolution of the correlation function and bias at small (down to $\sim 100 h^{-1}$ kpc) scales. We find that at all epochs the two-point correlation function of galaxy-size halos ξ_{hh} is well approximated by a power law with slope $\approx 1.6\text{--}1.8$. The difference between the shape of ξ_{hh} and the shape of the correlation function of matter results in the scale-dependent bias at scales $\lesssim 7 h^{-1}$ Mpc, which we find to be a generic prediction of the hierarchical models, independent of the epoch and of the model details. The bias evolves rapidly from a high value of $\sim 2\text{--}5$ at $z \sim 3\text{--}7$ to the antibias of $b \sim 0.5\text{--}1$ at small $\lesssim 5 h^{-1}$ Mpc scales at $z = 0$. Another generic prediction is that the comoving amplitude of the correlation function for halos above a certain mass evolves non-monotonically: it decreases from an initially high value at $z \sim 3\text{--}7$, and very slowly increases at $z \lesssim 1$. We find that our results agree well with existing clustering data at different redshifts, indicating the general success of the hierarchical models of structure formation in which galaxies form inside the host DM halos. Particularly, we find an excellent agreement in both slope and the amplitude between $\xi_{\text{hh}}(z = 0)$ in our Λ CDM₆₀ simulation and the galaxy correlation function measured using the Automatic Plate Measuring Facility galaxy survey. At high redshifts, the observed clustering of the Lyman-break galaxies is also well reproduced by the models. We find good agreement at $z \gtrsim 2$ between our results and predictions of the analytical models of bias evolution. This indicates that we have a solid understanding of the nature of the bias and of the processes that drive its evolution at these epochs. We argue, however, that at lower redshifts the evolution of the bias is driven by dynamical processes inside the nonlinear high-density regions such as galaxy clusters and groups. These processes do not depend on cosmology and tend to erase the differences in clustering properties of halos that exist between cosmological models at high z .

Subject headings: cosmology: theory — galaxies: halos — large-scale structure of universe — methods: n -body simulations

1. INTRODUCTION

It is widely believed that the distribution of galaxies is different from the overall distribution of dark matter (DM). This difference, the bias, is crucial for comparisons between observations and predictions of cosmological models. Observations provide information about the distribution of objects such as galaxies and galaxy clusters. The models, however, most readily predict the evolution of the DM distribution, which cannot be observed directly. The models, therefore, should be able to predict the distribution of objects or, conversely, predict how this distribution is different from that of the DM (i.e., the bias). The notion of bias was introduced by Kaiser (1984) to explain the large difference in clustering strength between galaxies and Abell clusters. Later, Kaiser (1986) and Bardeen (1986) applied this argument to galaxies themselves. Davis et al. (1985) showed that the cold dark matter (CDM) model disagreed with observations, if galaxies were distributed like DM. However, if a biased galaxy formation scenario was

assumed, the “galaxy” correlations substantially exceeded the correlations of mass at all scales and agreed with observations for certain values of bias. This work was followed by other studies which tried to account for the phenomenon of galaxy bias (e.g., Rees 1985; Schaeffer & Silk 1985; Silk 1985; Dekel & Silk 1986).

The bias can be defined and understood differently. In this paper we will use the conventional statistical definition of the bias as the ratio of the correlation functions of objects and DM:

$$b^2(M, r, z) \equiv \frac{\xi_{\text{hh}}(M, r, z)}{\xi_{\text{dm}}(r, z)}. \quad (1)$$

Here b^2 is the square of the bias function and $\xi_{\text{hh}}(M, r, z)$ and $\xi_{\text{dm}}(r, z)$ are the two-point spatial correlation functions of objects (halos in this study) and DM, respectively. Dependencies in the above equation indicate that in general the bias may depend on the epoch z , scale r , and properties of the objects such as their mass M . It is also expected that

the functional form $b^2(M, r, z)$ depends on the cosmological model. The bias in the above definition is most closely related to the observations because the observed $\xi_{\text{gg}}(M, r, z)$ can be compared with the $\xi_{\text{dm}}(r, z)$ predicted within a framework of a given cosmological model. This gives an estimate of the amount of bias needed for a cosmological model to agree with observations. While it is clear that this approach cannot be used to test a model, it provides some insights into the nature of bias and its evolution. For example, Steidel et al. (1998) used the observed clustering strength of high-redshift ($z \approx 3$) Lyman-break galaxies to derive the implied value of bias in different cosmological models. This value was found to be quite large in all models ($b \sim 3-6$). On the other hand, a number of theoretical studies (e.g., Klypin, Primack, & Holtzman 1996; Cole et al. 1997; Jenkins et al. 1998 and references therein) estimated ξ_{dm} in different cosmological models at $z = 0$ and made comparisons with accurate measurements of ξ_{gg} from local galaxy surveys. These studies indicate that significant antibias ($b < 1$) is required for the open and flat low- Ω_0 models at scales $\lesssim 3-8 h^{-1}$ Mpc, while $\Omega_0 = 1.0$ cluster-normalized models indicate positive bias ($b > 1$). Comparison of the low- and high- z results implies that, regardless of cosmological model, the bias has decreased significantly from the early epochs to the present.

The distribution of the DM and $\xi_{\text{dm}}(r, z)$ cannot be observed directly. Therefore, a test of a cosmological model is possible only if the model can predict the ξ_{gg} of observed objects. Unfortunately, this is not an easy and straightforward task. First of all, we should fully understand what are the observed objects and where/how they form. The standard lore is that observed galaxies form dissipatively inside DM halos. The properties of galaxies will then depend on the mass of the parent halo, its spin, details of dissipative processes and mass accretion history, and other factors (e.g., Mo, Mao, & White 1998). Therefore, in order to predict the type of galaxy and its properties, the relevant processes must be included in the model. However, it seems likely that in every sufficiently massive ($M \gtrsim 10^{11} h^{-1} M_\odot$) gravitationally bound halo baryons will cool, form stars, and produce an object resembling a galaxy (e.g., Kauffmann, White, & Guiderdoni 1993; Kauffmann, Nusser, & Steinmetz 1997; Roukema et al. 1997; Yepes et al. 1997; Salucci & Persic 1997). The galaxy population as a whole can be then viewed as a population of galaxy-size DM halos.¹ The clustering of the latter can be studied without the inclusion of complicated physics; it has been modeled using both direct numerical simulations and analytical methods.

Typical ingredients of the analytical models (e.g., Matarrese et al. 1997; Moscardini et al. 1998; Mann, Peacock, & Heavens 1998) are the extended Press-Schechter formalism (Bower 1991; Bond et al. 1991) used to follow mass evolution of halos, analytical approximations to the nonlinear clustering evolution of the DM (e.g., Hamilton et al. 1991; Peacock & Dodds 1994, 1996; Jain, Mo, & White 1995; Smith et al. 1998), and a model for bias evolution (e.g., Mo & White 1996; Matarrese et al. 1997). The evolution of bias in such models can be calculated quickly which makes

extensive parameter space studies possible. The main disadvantages are the large uncertainties (especially at small, $r \lesssim 5 h^{-1}$ Mpc, scales) introduced by bias prescriptions and limited applicability of the nonlinear clustering approximations.

Direct numerical simulations should, ideally, predict halo-halo clustering without any additional assumptions and uncertainties. However, until very recently the predictions of numerical simulations were also quite uncertain. The main reason for the uncertainty was that dissipationless n -body simulations had been consistently failing to produce galaxy-size DM halos in dense environments typical for galaxy groups and clusters. Recently, it was shown that this effect, known as “the overmerging problem” (e.g., Frenk et al. 1988; Summers, Davis, & Evrard 1995), is due mainly to the insufficient force and mass resolution of such simulations (Moore, Katz, & Lake 1996; Klypin et al. 1998, hereafter KGKK; Ghigna et al. 1998). The lack of sufficient resolution leads to artificial disruption of halos in clusters. This, in turn, leads to a strong artificial antibias (especially at small scales $\lesssim 3 h^{-1}$ Mpc, but larger scales are also affected). There are several ways to deal with this problem. One possible way is to break up massive structureless halos into subhalos using some kind of observationally motivated prescription (e.g., Nolthenius, Klypin, & Primack 1997; Klypin, Nolthenius, & Primack 1997). These subhalos can then be included into halo catalogs used to compute the correlation function and other halo statistics. Another common approach is to overcome overmerging by weighting the massive halos according to their mass and thus compute a weighted correlation function (e.g., Bagla 1998). Both of these approaches are useful. Nevertheless, it is not clear whether the unavoidable heuristic assumptions correctly take the processes driving the small-scale bias evolution into account. The weighting technique, for example, ignores the real physical effects in groups and clusters such as tidal stripping and dynamical friction. We will argue below that these effects are likely to be driving the small-scale bias evolution at low ($z \lesssim 1$) redshifts.

Hydrodynamic simulations that include gas cooling are affected by overmerging to a significantly lesser degree (e.g., Summers et al. 1995; Katz, Hernquist, & Weinberg 1999). The cooling creates compact dense objects inside halos which can survive in clusters. These simulations, therefore, can be used to study the halo clustering directly. Unfortunately, the computational cost required to simulate a large volume with sufficiently high mass resolution is prohibitively high. Moreover, such simulations usually oversimplify the gasdynamic by including only the cooling mechanism. This leads to “overcooling;” without a heating process to regulate it, the cooling produces very compact and dense baryonic blobs in the halo centers. These blobs do survive successfully in clusters, but they also suffer much less from the tidal stripping of material as compared with a realistic galaxy with a more extended distribution of baryons. The mass of the objects may thus be higher than it should be which may lead to excessive dynamical friction and thus incorrect dynamics of halos.

The very high resolution n -body simulations are thus a viable alternative, if the required resolution can be reached at an affordable computational cost. Analytical arguments and numerical experiments (Moore et al. 1996; KGKK) indicate that the required force and mass resolution are

¹ Nevertheless, it should be kept in mind that all of the relevant physics, such as star formation, supernovae feedback, and photoionization, must be included in order to model properly the properties of galaxies. Without such modeling the observational selection effects can be reproduced only approximately.

$\approx 1\text{--}2 h^{-1}$ kpc and $\lesssim 10^9 h^{-1} M_{\odot}$, respectively. This force resolution is sufficiently high for most halos to survive in high-density regions. The mass resolution is determined by the requirement that a galaxy-size halo have $\gtrsim 100$ particles to avoid relaxation effects and to assure a robust identification by a halo-finding algorithm. The numerical simulations that reach such resolution (Ghigna et al. 1998; KGKK) show that most halos do survive even in the richest clusters. The dynamic range required to reach the needed resolution in a statistically large volume, $\sim 50\text{--}100 h^{-1}$ Mpc, is quite high: $(2\text{--}5) \times 10^4$. Nevertheless, the advances in computer hardware and in the numerical algorithms now make it possible to carry out such simulations at an affordable computational cost. In this paper we use such high dynamic range simulations to calculate the two-point correlation function of halos and the corresponding bias using *all* halos in the simulated volume, i.e., both isolated DM halos and satellites of massive halos and halos inside group- and cluster-size systems. The simulations of different cosmological models and box sizes were made using the Adaptive Refinement Tree (ART) (Kravtsov, Klypin, & Khokhlov 1997) and the AP³M (Couchman 1991) n -body codes. The absence of the overmerging² in these simulations means that the additional steps such as the breaking-up of clusters or mass weighting (see above) are not necessary. Therefore, the correlation function of halos is measured *directly* down to unprecedentedly small scales ($\approx 150 h^{-1}$ kpc) without the usual uncertainties associated with these steps. For the first time this opens up the possibility of studying the effects of dynamical processes such as tidal destruction and dynamical friction on the evolution of small-scale bias. The results on the evolution of bias and on the halo correlation function can be used as a basis for comparisons and interpretations of the existing and upcoming observations, as well as a check and/or input for the analytic models of clustering evolution.

The paper is organized as follows. In § 2 we briefly review the definitions of bias and current analytical models of its evolution. The cosmological models studied in this paper are described in § 3. The details of the numerical simulations and discussion of the construction of halo catalogs and halo survival in the high-density regions is given in § 4. In § 5 we present our results on the evolution of halo clustering and bias in different cosmological models. We also present a comparison of our $z = 0$ results with the galaxy correlation function measured using the Automatic Plate Measuring Facility (APM) galaxy survey. A discussion of the main results is presented in § 6. We summarize our main results and conclusions in § 7.

2. THE NOTION OF BIAS

The notion of bias is more complicated than equation (1) might suggest. Formally, the bias is defined as a function relating fluctuations in the DM density, δ_{dm} , to the fluctua-

² The extent to which the very central regions ($r \lesssim 200 h^{-1}$ kpc) of clusters are affected by the overmerging, even with resolution this high, is still a matter of debate. Ghigna et al. (1998), for example, argue that these regions are still completely overmerged. They find, however, that halos survive at smaller radii ($\approx 50 h^{-1}$ kpc) in their 5 kpc resolution RUN1, as compared with the 10 kpc RUN2. The resolution of the simulations presented in this paper is comparable to the RUN1. We do find halos within the central $\approx 100 h^{-1}$ kpc (see § 4.3 and Figs. 1–3). Although some halos do survive at $r \approx 100 h^{-1}$ kpc from cluster center, our tests show that these regions may be affected by the overmerging. The larger scales $\gtrsim 100 h^{-1}$ kpc are not affected

tions in the number density of objects, δ_n . In general, this relationship can be complicated and may depend on a large number of factors: scale, mass and/or type of objects, time, etc. The large number of the dependencies or discreteness of the object distribution can result in the stochasticity of the bias (Dekel & Lahav 1999): a scatter in the relationship between δ_n and δ_{dm} . Finally, the bias can be nonlocal, if the probability of forming an object at a given point is not fully determined by local factors. For example, in addition to the local density, temperature, etc. (see, e.g., Blanton et al. 1999), the probability of forming a galaxy may depend on environment. Analytical results of Catelan et al. (1998a) indicate that the bias is expected to be nonlocal even in the linear regime.

The lack of general understanding of these dependencies of the bias usually results in the use of the simplest assumptions. The most common approach is to assume that bias is local, depends only on the local matter density, and is linear: $\delta_n = b\delta_{\text{dm}}$. An obvious consequence of the latter assumption is that bias is scale independent. In this case, the correlation function and power spectrum of halos and DM are simply related by a constant scaling factor. Although the linearity of bias would greatly simplify the theoretical interpretation of the clustering data, it is likely that bias depends on a variety of processes that may lead to nonlinearity. These processes include merging, tidal disruption (e.g., Dubinski 1998), suppression of galaxy formation in small halos due to supernovae feedback (Dekel & Silk 1986; Yepes et al. 1997), etc.

The observations, in fact, indicate that at small scales galactic bias is nonlinear. The correlation functions of different types of galaxies differ in amplitude and shape suggesting that at least some of the galaxies are nonlinearly biased. Theoretical predictions, depending on the model and method of analysis, range from (almost) constant bias (e.g., Peacock & Dodds 1994, 1996; Kauffmann et al. 1997), to positive and decreasing with scale bias (e.g., Cen & Ostriker 1992; Cen, Gnedin, & Ostriker 1993; Blanton et al. 1999), to the scale-dependent increasing with scale antibias (Klypin, Primack, & Holtzman 1996; Jenkins et al. 1998). The differences can be typically traced either to different physical processes accounted for in analyses (or lack thereof) or to a different way of treating observational data. For example, Cen & Ostriker (1992) predict that galaxies in the CDM model should be positively biased and the bias should decrease with the scale. However, the numerical resolution of these simulations has been too crude to allow for galaxy survival in high-density regions, and the results may be affected by this. We should note that galaxy bias actually *must* be scale dependent in some of the models. Klypin et al. (1996) and Jenkins et al. (1998) compared the correlation function of the DM with the correlation function of galaxies in the APM survey. The comparison shows that antibiased distribution of galaxies must be *antibiased* and scale dependent in the Λ CDM model.

During the last years, significant progress has been made in the analytical modeling of the bias and its evolution (e.g., Coles 1993; Fry 1996; Mo & White 1996, hereafter MW; Matarrese et al. 1997; Mann et al. 1998; Catelan, Matarrese, & Porciani 1998b; Catelan et al. 1998a). Although the current analytical models may have some drawbacks and limitations, they provide an insight and interpretation for numerical simulations. At this point it is also important to check how well the prediction of the analytical models

agrees with the results of simulations (see, e.g., MW; Mo, Jing, & White 1996; Jing 1998). We will therefore briefly review some results of the analytical models concerning evolution of the bias.

In a seminal paper, Kaiser (1984) showed that if the observed systems in the universe (such as galaxies and galaxy clusters) form in the peaks of the density field, their distribution is biased. This is an example of statistical bias, the bias determined simply by the fact that objects do not sample the distribution of matter but that of the peaks, the latter having a statistically different distribution from the former. Thus, the bias is introduced from the start by the way the objects form. However, the bias subsequently changes as the distribution evolves driven by the gravitation. In hierarchical models this evolution results in growth of objects via multiple mergers. However, if the merger rate is low, the evolution of bias can be modeled by the object-conserving model. In this model the objects form with an initial statistical bias, and after that are dragged without merging by a gravitational pull from the surrounding density fluctuations (Dekel & Rees 1987; Nusser & Davis 1994; Fry 1996; Tegmark & Peebles 1998).

MW used the extended Press-Schechter formalism to derive an expression for the bias in Lagrangian coordinates³ (comoving radius R of the region from which halos form or halo mass M). At linear scales, this expression⁴ for the bias at redshift z for DM halos of mass M formed at redshift z_f is (Matarrese et al. 1997)

$$b(M, z | z_f) = 1 + \frac{v^2 - 1}{\delta_f}. \quad (2)$$

Here $\delta_f = \delta_c D_+(z)/D_+(z_f)$, $D_+(z)$ is the growing mode of linear perturbations normalized to unity at $z = 0$, $v = \delta_f/\sigma(M, z)$, δ_c is the critical overdensity for spherical collapse at $z = 0$, and $\sigma(M, z)$ is the rms linear mass fluctuation on the scale M of halos linearly extrapolated to redshift z . This expression is similar to that obtained in earlier studies from a peak-background split argument (e.g., Cole & Kaiser 1989). The standard interpretation of the Press-Schechter description of the hierarchical evolution is that at any epoch z all halos merge immediately to form more massive halos. Thus, if observed objects are identified with host halos at any epoch, then $z = z_f$ in equation (2). Matarrese et al. (1997) call this the merging model. The object-conserving and merging models are two extreme pictures of clustering evolution, although they may be applicable to the evolution

³ More sophisticated analytical treatment of bias in Lagrangian coordinates can be found in Catelan et al. (1998a) and Mann et al. (1998).

⁴ MW note that eq. (3) should be valid even when $\delta_{\text{dm}} \gtrsim 1$ or $\xi_{\text{dm}}(r) \sim 1$, as long as the scale r is larger than the Lagrangian radius R . They find that at these scales the correlation function of halos and the bias in their numerical simulations are well described by eq. (3) (see, however, Catelan et al. 1998b and Jing 1998).

of galaxy clustering at certain epochs. At some epochs the halos may neither survive nor merge instantly. Moreover, other processes such as halo dynamics in galaxy clusters and groups may become important when clustering reaches highly nonlinear stages. The wealth of potentially important processes may make a one-to-one identification between galaxies⁵ and DM halos very difficult (see, for example, the discussion by Moscardini et al. 1998).

Equation (2) gives an estimate of the bias for objects of a single mass. The bias of a sample of objects (“effective” bias⁶) with a range of masses $M > M_{\text{min}}$ should be calculated as a weighted average over the mass distribution of objects $n(M, z)$:

$$b_{\text{eff}}(z) = n(z)^{-1} \int_{M > M_{\text{min}}} b(M, z | z_f) n(M, z) d \ln M, \quad (3)$$

where $n(M, z)$ is given by the Press-Schechter (1974) distribution and $n(z)$ is the mean number density of objects with masses $M > M_{\text{min}}$ at redshift z . Note that the bias weighted in this way will give a correct value only for the bias estimated from point-to-point comparisons of halo and matter overdensities $b = \delta_h/\delta_m$. For the spatially averaged bias calculated using correlation functions or power spectra, the weighting will not give a correct value because of the cross terms resulting from squaring the overdensities. Moscardini et al. (1998) give a useful fitting formula for $b_{\text{eff}}(z)$,

$$b_{\text{eff}}(z) = 1 - 1/\delta_c + [b_{\text{eff}}(0) - 1 + 1/\delta_c]/D_+(z)^\beta, \quad (4)$$

and provide best-fit parameters $b_{\text{eff}}(0)$ and β for a variety of different cosmological models and values of M_{min} . The generic feature of the evolution of the effective bias described by equation (3) is its rapid decrease with decreasing redshift and increase with increasing M_{min} . For galaxy-size halos, $b_{\text{eff}}(0) \sim 0.5-1.0$ and $\beta \sim 2.0-1.7$ for $M_{\text{min}} \sim 10^9-10^{12} h^{-1} M_\odot$. This gives $b_{\text{eff}} \sim 2-4$ at $z = 3$ and $b_{\text{eff}} \sim 0.5-1.0$ at the present epoch. We will use equation (4) in § 6 to interpret and compare our results with predictions of the analytical models discussed above.

3. COSMOLOGICAL MODELS

We have chosen to study the evolution of bias in four representative variants of the CDM models (see details in Table 1): (1) the standard *COBE*-normalized CDM model (SCDM); (2) a variant of the $\Omega_0 = 1.0$ CDM model (τ CDM) with a different shape of the power spectrum (the shape parameter $\Gamma = \Omega_0 h = 0.2$); (3) a flat low-density model with $\Omega_0 = 1 - \Omega_\Lambda = 0.3$ (Λ CDM); and (4) an open model with $\Omega_0 = 0.3$ (OCDM). The observations of the galaxy

⁵ The situation with the evolution of clusters of galaxies is, of course, much simpler.

⁶ We follow here the notation and terminology of Matarrese et al. (1997).

TABLE 1
COSMOLOGICAL MODELS

| Model | Ω_0 | $\Omega_{\Lambda,0}$ | h | t_0 (Gyr) | σ_8 | Approximation |
|----------------------------------|------------|----------------------|------|----------------|------------|-------------------|
| SCDM | 1.0 | 0.0 | 0.50 | 13.1 | 1.1 | Efstathiou et al. |
| OCDM | 0.3 | 0.0 | 0.65 | 12.2 | 0.9 | BBKS + Sugiyama |
| Λ CDM ₁ | 0.3 | 0.7 | 0.70 | 13.4 | 1.17 | BBKS + Sugiyama |
| Λ CDM ₂ | 0.3 | 0.7 | 0.70 | 13.4 | 1.0 | Klypin & Holtzman |
| τ CDM | 1.0 | 0.0 | 0.5 | 13.1 | 1.0 | Efstathiou et al. |

clustering indicate that the power spectrum of the galaxy distribution has a shape different from that of the standard CDM model: $\Gamma = \Omega_0 h \approx 0.2$ instead of $\Gamma = 0.5$ of the SCDM (e.g., Maddox, Efstathiou, & Sutherland 1996; Peacock & Dodds 1994). This has motivated Jenkins et al. (1998) to study the τ CDM model, in which τ indicates the fact that lower values of Γ may be obtained with a late decay of the massive τ -neutrino. The physics (additional to the physics of the SCDM model) responsible for the change of the shape is, in fact, irrelevant for the study of structure formation. Although the model in that respect is somewhat heuristic, it is interesting as an example of a model with $\Omega_0 = 1$ and an approximately correct shape of the power spectrum. The observations of the galaxy cluster evolution (Eke et al. 1998) and of the baryon fraction in clusters (Evrard 1997) strongly indicate a value of matter density $\Omega_0 \approx 0.3$, while various observational measurements of the Hubble constant (e.g., Kim et al. 1997; Falco et al. 1997; Salari & Cassisi 1998) tend to converge on the values of $h \approx 0.6$ – 0.7 . Therefore, we have considered two models (open and flat) with $\Omega_0 = 0.3$ and $h = 0.65$ – 0.7 . The age of the universe in all of our models is given in Table 1 and is in good agreement with the ages of the oldest globular clusters (Chaboyer 1998).

We have used different approximations for the power spectrum of density fluctuations for different considered models. For the OCDM and Λ CDM₁ models (see Table 1) we used the Bardeen et al. (1986, hereafter BBKS) fit for the power spectrum with corrections of Sugiyama (1995):

$$P(k) = AkT^2(k),$$

$$T(k) = \frac{\ln(1 + 2.34q)}{2.34q} [1 + 3.89q + (16.1q)^2 + (5.46q)^3 + (6.71q)^4]^{-1/4}, \quad (5)$$

$$q = k\{\Omega_0 h^2 \exp[-\Omega_b - \sqrt{2h(\Omega_b/\Omega_0)}]\}^{-1}, \quad (6)$$

where $\Omega_b = 0.0125 h^{-2}$ (Walker et al. 1991⁷) and k is in Mpc^{-1} . The power spectra for both the SCDM and the τ CDM models were approximated by the fitting formula of Efstathiou, Bond, & White (1992),

$$P(k) = \frac{Ak}{\{1 + [ak + (bk)^{3/2} + (ck)^2]^{1.13}\}^{2/1.13}}, \quad (7)$$

where $a = 6.4/\Gamma$, $b = 3.0/\Gamma$, $c = 1.7/\Gamma$, and A is the normalization constant. The shape parameter Γ is 0.5 and 0.2 for the SCDM and τ CDM models, respectively. These two analytic fits provide fairly good approximations to the power spectra of these models in the limit $\Omega_b/\Omega_0 \ll 1$.

For the Λ CDM₂ models we have used an approximation to the power spectrum different from that of the Λ CDM₁ model. The approximation

$$P(k) = \frac{Ak}{(1 - 1.5598k^{1/2} + 47.986k + 117.77k^{3/2} + 321.92k^2)^{2 \times 0.9303}} \quad (8)$$

is given by Klypin & Holtzman (1997) and was obtained by a direct fit to the power spectrum estimated using a Boltz-

mann code. The accuracy of this approximation is $\lesssim 2\%$ (see Klypin & Holtzman 1997 for details). A small shift in the normalization makes the approximations for the Λ CDM₁ and Λ CDM₂ models very similar in the range of wavenumbers probed in our simulations [$k \approx (0.1$ – $10) h \text{ Mpc}^{-1}$]. This shift can be expressed using the value of σ_8 (amplitude of fluctuations on $8 h^{-1} \text{ Mpc}$ scale): $\sigma_8 = 1.17$ for the BBKS approximation versus $\sigma_8 = 1.0$ for the Holtzman approximation. With these values of σ_8 the differences in power are negligible at large scales [$k \approx (0.1$ – $0.3) h \text{ Mpc}^{-1}$] and are within 10% at the smaller scales.

Our SCDM model was normalized to the 2 yr *COBE*-Differential Microwave Radiometer (DMR) data, $\sigma_8 = 1.1$ (a somewhat higher value, $\sigma_8 \approx 1.15$ – 1.2 , is obtained from the 4 yr *COBE*-DMR data; see, e.g., Bunn & White 1997). This normalization is inconsistent with the normalization, $\sigma_8 \approx 0.5$, deduced from the observed cluster abundances (e.g., Eke, Cole, & Frenk 1996), which reflects the well-known failure of this model to account for both *COBE* and cluster data. Our normalization of the OCDM is higher than that implied by the 4 yr *COBE*-DMR data ($\sigma_8 \approx 0.5$) but is consistent with the normalization, $\sigma_8 \approx 0.9$, implied by the cluster abundances. The normalization of our Λ CDM models, on the other hand, is in good agreement with both cluster and the 4 yr *COBE* data. As explained above, the small difference in normalization between the Λ CDM₁ and Λ CDM₂ was introduced to minimize differences between the two power spectrum approximations used in these models. Normalization of the τ CDM model is inconsistent with both the *COBE* normalization ($\sigma_8 \approx 0.45$) and with the cluster abundance normalization ($\sigma_8 \approx 0.52$). This is motivated by our intent to use τ CDM as a toy model rather than a reasonable approximation to the real universe. The normalization of the τ CDM is similar to normalizations of the CDM and Λ CDM models. Therefore, comparison between results of these models allows us to study the effects of changing the shape of the power spectrum and the value of Ω_0 . Finally, we note that the bias in $\Omega_0 = 1$ models with lower normalizations can be deduced approximately from our results at a redshift $z > 0$, such that $\sigma_8/(1+z)$ corresponds to the desired normalization.

4. THE NUMERICAL SIMULATIONS

4.1. Simulation Parameters

We have used two different n -body codes to carry out our simulations: ART (Kravtsov et al. 1997) and the AP³M code⁸ (Couchman 1991). Comparison of the results obtained with different numerical codes allows us to ensure that the results are robust. The AP³M code is an extension of the well-known P³M algorithm (Hockney & Eastwood 1981). The code performs hierarchical rectangular refinements in the high-density regions to reduce expensive particle-particle calculations. The gravitational force is obtained by matching the gravitational forces calculated using the fast Fourier transform solver on the base and refinement grids and the small-scale force calculated using direct particle-particle summation (see Couchman 1991 for details). A total of four refinement levels were allowed during the course of the AP³M simulations presented here. The ART code also reaches high force resolution by refining

⁷ For the Λ CDM₂ we used a slightly higher value of $\Omega_b = 0.015 h^{-2}$.

⁸ The original public code was modified slightly to take into account $\Omega_0 \neq 1$ models.

all high-density regions with an automated refinement algorithm. The refinements are recursive: the refined regions can also be refined, each subsequent refinement having half of the previous level's cell size. This creates a hierarchy of refinement meshes of different resolution covering the regions of interest. The refinement is done cell by cell (individual cells can be refined or derefined), and meshes are not constrained to have a rectangular (or any other) shape. This allows us to refine the required regions in an efficient manner. The criterion for refinement is local overdensity of particles: in the simulations presented in this paper the code refined an individual cell only if the density of particles (smoothed with the cloud-in-cell scheme; Hockney & Eastwood 1981) was higher than $n_{\text{th}} = 5$ particles. Therefore, all regions with overdensity higher than $\delta = n_{\text{th}} 2^{3L}/\bar{n}$, where \bar{n} is the average number density of particles in the cube, were refined to the refinement level L . For the two ART simulations presented here, ΛCDM_{60} and $\Lambda\text{CDM}_{30}^{\text{ART}}$, \bar{n} is $\frac{1}{8}$ and 1, respectively. The Poisson equation on the hierarchy of meshes is solved first on the base grid and then on the subsequent refinement levels. On each refinement level the code obtains potential by solving a Dirichlet boundary problem with boundary conditions provided by the already existing solution at the previous level. There is no particle-particle summation in the ART code. The detailed description of the code is given by Kravtsov et al. (1997). Note, however, that the present version of the code uses multiple time steps on different refinement levels, as opposed to the constant time stepping in the original version of the code. The multiple time stepping scheme is described in some detail by Kravtsov et al. (1998; also see below).

The information about the numerical parameters of the simulations is given in Table 2. The AP³M code was used to produce four simulations of different cosmological models⁹ with the box size $L_{\text{box}} = 30 h^{-1}$ Mpc. The size of the box side is a compromise between the requirements of the high spatial resolution ($\sim 2\text{--}4 h^{-1}$ kpc) and good statistics of halos. Nevertheless, for our most realistic model (ΛCDM) we also use the ART code to simulate a $60 h^{-1}$ Mpc box (ΛCDM_{60} run). We estimate the effects of the finite box size (see § 5.1) on our results by comparing the results of the $140 h^{-1}$ Mpc box simulation of Jenkins et al. (1998) with the results of our 60 and $30 h^{-1}$ Mpc boxes. All AP³M runs were done with 128^3 particles. The two ART runs used 256^3 particles. The initial conditions were set using the Zeldovich approximation on uniform 128^3 , 256^3 , and 512^3 meshes for the AP³M runs, the $\Lambda\text{CDM}_{30}^{\text{ART}}$ run, and the ΛCDM_{60} run,

⁹ Runs SCDM, ΛCDM_{30} , and τCDM have not been completed because of the high computational expense. The simulations were stopped at $z = 0.3$.

respectively. The seed used to generate the Gaussian random density field was the same in all of our AP³M runs but different for each of the two ART runs. All of the simulations are started at the moment of time when the rms density fluctuations at the Nyquist wavelength λ_{Nyq} are still linear: $\sigma(\lambda_{\text{Nyq}}, z_i) \sim 0.1\text{--}0.2$. All AP³M runs evolved during a period in which the linear growth factor increased by a factor of 50. This explains different values of z_{init} for different models in Table 2.

As was explained in § 1, the purpose of our study was to compute the correlation function and the bias accounting for all DM halos, including those inside groups and clusters. To assure that halos do survive in clusters the force resolution should be $\sim 1\text{--}3 h^{-1}$ kpc (Moore et al. 1996; KGKK). Furthermore, if we aim to study galaxy-size halos, the mass resolution should be $\lesssim 10^9 h^{-1} M_{\odot}$ to resolve galaxy-size halos ($M \gtrsim 10^{11} h^{-1} M_{\odot}$) with at least ≈ 100 particles. The compromise between these considerations and the computational expense determined the force and mass resolution of our simulations (see Table 2). The ART code integrates the equations of motion in comoving coordinates. However, the refinement strategy of the ART code is designed to effectively preserve the initial physical resolution of the simulation (see below). The peak resolution is reached by creating a refinement hierarchy with six levels of refinement. In the AP³M runs the force resolution η (spline-softening length) was kept constant in comoving coordinates while fluctuations are still in the linear regime and is then set to be constant in physical units. The switch occurs at the moment when the first galaxy-size halos start to collapse ($z \sim 5\text{--}10$) for our simulations. We chose to maintain a fixed comoving resolution until it reaches $\sim 3 h^{-1}$ kpc (physical) (at $\sim 5\text{--}10$). At later moments the resolution is fixed to this value in physical coordinates (the exception is the OCDM model in which the resolution was set to $4.7 h^{-1}$ kpc by mistake). The dynamical range L_{box}/η of the simulations implied by the force resolution is $\approx 16,000$ (32,000 formal) for the ART runs and 6000–10,000 for the AP³M runs. The dynamic range of the AP³M runs is just enough to keep the initial physical resolution ($\approx 2\text{--}5 h^{-1}$ kpc). The ART code integrates the evolution in comoving coordinates. Therefore, in order to prevent degradation of force resolution in physical coordinates, the dynamic range between the start and the end ($z = 0$) of the simulation should increase by $(1 + z_i)$, i.e., for our simulations to reach $512 \times (1 + z_i) = 15,872$. This is accomplished with the prompt successive refinements during the simulations.

The time stepping of the AP³M and ART codes is rather different. First of all, the codes integrate the equation of motion using different time variables: the time in the AP³M

TABLE 2
PARAMETERS OF SIMULATIONS

| Code | Model | Run | z_{init} | m_{particle} ($h^{-1} M_{\odot}$) | N_{steps} | Resolution (kpc h^{-1}) | Box (Mpc h^{-1}) | N_{part} |
|------------------------|-----------------------|---------------------------------------|-------------------|---|--------------------|-------------------------------|------------------------|-------------------|
| AP ³ M..... | SCDM | SCDM | 49 | 3.5×10^9 | 8000 | 3.0 | 30 | 128^3 |
| AP ³ M..... | OCDM | OCDM | 109 | 1.1×10^9 | 7000 | 4.7 | 30 | 128^3 |
| AP ³ M..... | ΛCDM_1 | ΛCDM_{30} | 64 | 1.1×10^9 | 4000 | 3.0 | 30 | 128^3 |
| ART | ΛCDM_2 | ΛCDM_{60} | 30 | 1.1×10^9 | 41300 | 1.8 | 60 | 256^3 |
| ART | ΛCDM_2 | $\Lambda\text{CDM}_{30}^{\text{ART}}$ | 45 | 1.3×10^8 | 13800 | 0.9 | 30 | 256^3 |
| AP ³ M..... | τCDM | τCDM | 50 | 3.5×10^9 | 8000 | 3.0 | 30 | 128^3 |

code and the expansion factor in the ART code. In the AP³M runs the time step is constant and is the same for all particles. In the ART runs, as was noted above, the particles residing on different refinement levels move with different time steps. The particles on the same level, however, move with the same step. The refinement of the time integration mimics spatial refinement, and the step for each subsequent refinement level is 2 times smaller than the step on the previous level. The global time step hierarchy is thus set by the step Δa_0 at the zeroth level (uniform base grid). The step on level L is then $\Delta a_L = \Delta a_0/2^L$. The choice of an appropriate time step for a simulation is dictated by the adopted force resolution. The number of time steps in our simulations is such that the rms displacement of particles during a single time step is always less than $\eta/4$ (less than $\frac{1}{4}$ of a cell in the ART code).¹⁰ The size of the time step, Δt , for the AP³M runs was chosen to be sufficiently small to satisfy the stability criteria of the numerical integration (e.g., Efstathiou et al. 1985) throughout the entire run. In the case of ART runs, the value of $\Delta a_0 = 0.0015$ was determined in a convergence study using a set of smaller 64³ particle simulations described by Kravtsov et al. (1998). In both AP³M and ART runs the energy was conserved with an accuracy $\lesssim 1\%$.

4.2. Identification of Halos

Identification of DM halos in the very high density environments (e.g., inside groups and clusters) is a challenging problem. Traditional halo-finding algorithms, such as friends-of-friends (e.g., Davis et al. 1985) or “overdensity-200” (e.g., Lacey & Cole 1994), cannot be used. These algorithms are not designed to search for substructure; they identify an isolated halo above virial overdensity as a single object and cannot account for the internal substructure. Our goal, however, is to identify both isolated halos and halos orbiting within larger systems (“subhalos”). The problems associated with halo identification within high-density regions are discussed by KGKK. In this study we use a halo-finding algorithm called bound density maxima (BDM) (see KGKK). A detailed description of the working version of the BDM algorithm used here can be found in Klypin & Holtzman (1997). Other recently developed algorithms capable of identifying satellite halos are described by Ghigna et al. (1998) and KGKK. The main idea of the BDM algorithm is to find positions of local maxima in the

¹⁰ Note, however, that the distance traveled by the fastest moving particle in one time step in AP³M runs can be larger than η , especially at late times and in the Λ CDM₃₀ run. In the ART code, particles do not move further than ~ 0.5 cells in a single time step, where the cell size and time step for particles located on the refinement level L are $\Delta x_0/2^L$ and $\Delta a_0/2^L$, respectively.

density field smoothed at a certain scale and to apply physically motivated criteria to test whether the identified site corresponds to a gravitationally bound halo. In the following we describe the specific parameters of the BDM used to construct the halo catalogs used in our study (the main parameters are listed in Table 3).

The radius of a halo assigned to it by the algorithm is either its virial radius¹¹ or $150 h^{-1}$ kpc, whichever is smaller. The latter is approximately the maximum virial radius we would expect for a galaxy-size halo. The mass and radius are very poorly defined for the satellite halos because of the tidal stripping which alters a halo’s mass and physical extent. Therefore, in this study we will use maximum circular velocity V_{\max} as a proxy for halo mass. This allows us to avoid complications related to the mass and radius determination for satellite halos. For isolated halos, V_{\max} and the halo’s virial mass are directly related. For example, for a halo with a density distribution described by the Navarro, Frenk, & White (1996, hereafter NFW) profile $\rho(r) \propto x^{-1}(1+x)^{-2}$ ($x \equiv r/R_s$; R_s is scale-radius),

$$V_{\max}^2 = \frac{GM_{\text{vir}}}{R_{\text{vir}}} \frac{c}{f(c)} \frac{f(2)}{2}, \quad (9)$$

where M_{vir} and R_{vir} are virial mass and radius, $f(x) \equiv \ln(1+x) - x/(1+x)$, and $c \equiv R_{\text{vir}}/R_s$. While for the subhalos V_{\max} may not be related to mass in any obvious way, it is still the most physically and observationally motivated halo quantity. The limiting radius of $150 h^{-1}$ kpc is sufficient to determine the V_{\max} for galaxy-size halos. The cluster-size halos are not explicitly excluded from the halo catalogs. We assume therefore that the center of each cluster can be associated with a central cluster galaxy. The latter (because of the lack of hydrodynamics and other relevant processes) cannot be identified in our simulations in any other way.

The density maxima are identified using a top-hat filter with radius r_s (“search radius”). The search is performed starting from a large number of randomly placed positions (“seeds”) and proceeds by iteratively moving the center of mass within a sphere of radius r_s until convergence. In order to make sure that we use a sufficiently large number of seeds, we used the position of every 10th particle as a seed. Therefore, the number of seeds by far exceeds the number of expected halos. The search radius r_s also defines the minimum allowed distance between two halos. If the distance between centers of any of the two halos is less than $2r_s$, only one halo (the more massive of the two) is left in the

¹¹ The virial overdensity δ_{TH} is set in accord with the prediction of the top-hat collapse model. Note that δ_{TH} depends on the cosmological model (e.g., Kitayama & Suto 1996).

TABLE 3
PARAMETERS OF HALO-FINDING ALGORITHM

| Run | $\bar{\delta}_{\text{TH}}$ | M_{min} ($h^{-1} M_{\odot}$) | r_s (kpc h^{-1}) |
|--|----------------------------|--|--------------------------|
| SCDM | 180 | 7×10^{10} | 13 |
| OCDM | 180-400 | 2×10^{10} | 13 |
| Λ CDM ₃₀ | 180-340 | 2×10^{10} | 13 |
| Λ CDM ₆₀ | 180-340 | 10^{10} | 20 |
| Λ CDM ₃₀ ^{ART} | 180-340 | 10^9 | 10 |
| τ CDM | 180 | 7×10^{10} | 13 |

catalog. A typical value for the search radius is $(10\text{--}20) h^{-1}$ kpc. We set a lower limit for the mass inside the search radius $M(<r_s)$: halos with $M(<r_s) < M_{\min}$ are not included in the catalog. This is done to exclude pure Poisson fluctuations from the list of halo candidates. Some halos may have significant substructure in their cores due, for example, to an incomplete merger. Such cases appear in the catalogs as multiple (2–3) halos with very similar properties (mass, velocity, radius) at small separations. Our strategy is to count these as a single halo. The specific criteria used to identify such cases require that (1) the distance between halo centers is $\lesssim 150 h^{-1}$ kpc, (2) their relative velocity in units of the rms velocity of particles in the halos $\Delta v/v$ is less than 0.15, and (3) the difference in mass is less than factor 1.5. Only the most massive halo is kept in the catalog.

It is obvious that for a statistical study it is important to be confident that our BDM algorithm does not miss a large fraction of halos. While a substantial effort is made to reject fake halos, it is important to make sure that all real halos are included in the catalog. The algorithm is very efficient at finding isolated halos, and the major difficulties are in the identification of halos in crowded regions. Halo identification in such regions is complicated by the large number of halos and by the high-density background of fast-moving particles. Therefore, performance of the algorithm in such

regions is a good indicator of its overall performance. In fact, the parameters of the halo finder used to construct our halo catalogs were tuned by visual inspections of the most difficult and complicated regions. An example of such regions is shown in Figure 1. The figure shows the distribution of the DM particles in a Virgo-type cluster¹² in the Λ CDM model (Λ CDM₆₀ run). To enhance the substructure, particles are color coded on a gray scale with a rendering algorithm based on the local particle density (see Fig. 1, *legend*). A large number of distinct and compact DM halos is clearly present within the virial radius of the cluster. Figure 2 shows the positions of DM halos identified by the BDM code in the same volume. There are 121 halos in the plot, each halo having more than 20 bound particles. More stringent limits of more than 30 particles and a maximum circular velocity, V_{\max} , larger than 80 km s^{-1} produce 98 halos. All distinct halos visible in Figure 1 are identified.

4.3. Survival of Halos in Clusters

In § 1 we stressed that the main new feature of the analysis presented in this paper is the identification and use of halos located inside the virial radius of other halos (satellites or subhalos). Particularly, one of the main goals is

¹² The distribution of matter and halos in this cluster is discussed in the next section.

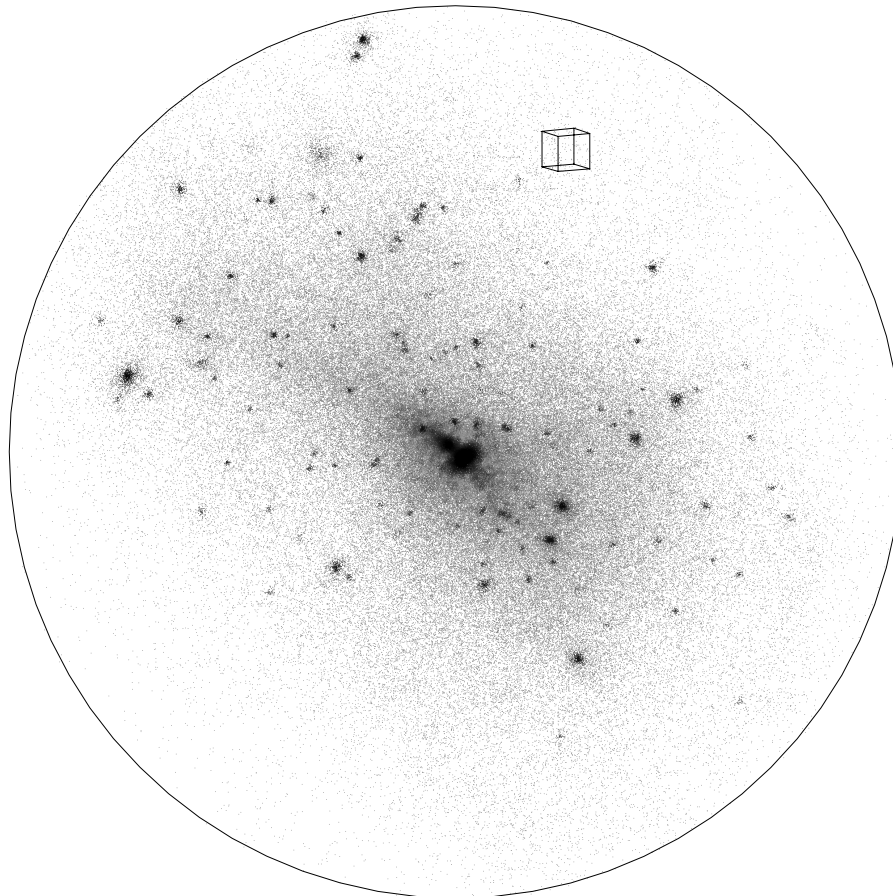


FIG. 1.—Distribution of DM in a Virgo-like cluster in the Λ CDM₆₀ simulations. The cluster virial mass is $2.45 \times 10^{14} h^{-1} M_{\odot}$, and the corresponding three-dimensional velocity dispersion is $\approx 1022 \text{ km s}^{-1}$. The particles inside a sphere of the radius of $1.5 h^{-1} \text{ Mpc}$ (solid circle) are shown. The size of the small box, shown to provide the comparison scale, is $100 h^{-1} \text{ kpc}$. To enhance the contrast, we have color coded DM particles on a gray scale according to their local density; the intensity of each particle is scaled as the logarithm of the density difference $\rho_{15} - \rho_{75}$, where the densities were obtained using top-hat filter with radii 15 and $75 h^{-1} \text{ kpc}$.

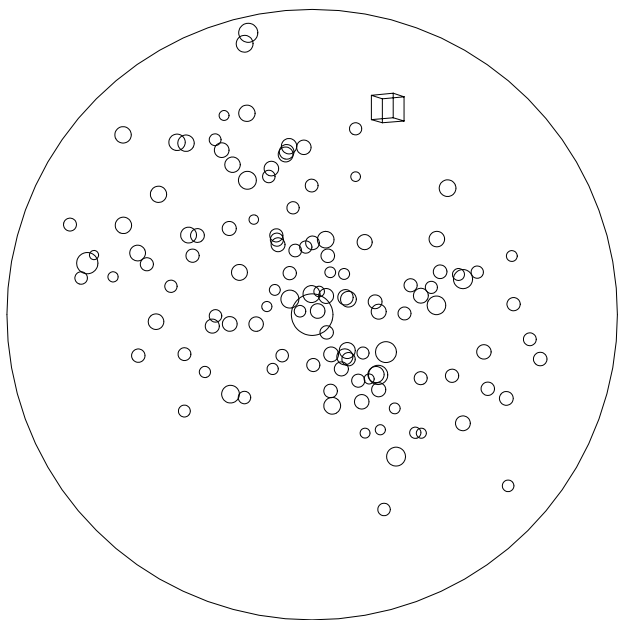


FIG. 2.—Region of the space shown in Fig. 1 with circles representing the DM halos found by the BDM halo finder. The area of each circle representing a halo is proportional to the halo’s maximum circular velocity. There are 121 halos in the plot, each of which has mass greater than $2 \times 10^{10} h^{-1} M_{\odot}$ (more than 20 bound particles).

to include halos inside cluster-size halos. This would allow an estimation of the halo-halo correlation function down to unprecedentedly small scales ($\sim 150 h^{-1}$ kpc). However, we can consider this estimate robust only if we are confident that no halos (or a very small fraction of them) are artificially destroyed in clusters because of the insufficient resolution. KGKK have discussed analytical estimates and numerical experiments that could be used to address this issue. Following the approach of KGKK, we have run a series of small n -body simulations¹³ using the direct-summation Aarseth’s code (Binney & Tremain 1987). The basic setup of the simulations is as follows. A DM halo of virial mass $10^{12} h^{-1} M_{\odot}$ (containing a few thousand particles within the virial radius) is constructed. The initial equilibrium density profile of the halo is described by the NFW formula. The halo is then placed on an orbit in a constant potential corresponding to a galaxy cluster of mass $2 \times 10^{14} h^{-1} M_{\odot}$ with the NFW density distribution. The particular numbers quoted here are intended to mimic the orbital evolution in the cluster presented in Figures 1–3. The orbital evolution of the halo was studied for different orbits and different (mass and force) resolutions. Both the mass and the force resolution were varied by more than a factor of 10. The orbital evolution of mass bound to the halo converges at the force resolution¹⁴ $\approx 3\text{--}4 h^{-1}$ kpc, i.e., the evolution of bound mass in runs with higher resolution is *identical*. In fact, during the first ≈ 5 Gyr the resolution of $\approx 10 h^{-1}$ kpc is adequate. The mass loss in this case is somewhat higher which leads to total destruction after 5 Gyr, whereas a resolution of $3 h^{-1}$ kpc allows the halo to survive during the Hubble time. These experiments have

¹³ Similar to those of KGKK, but with all parameters appropriate for the Λ CDM model.

¹⁴ Here we quote all resolutions for the spline kernel η of the AP³M; the corresponding resolution is $\approx \eta/2$ for the ART.

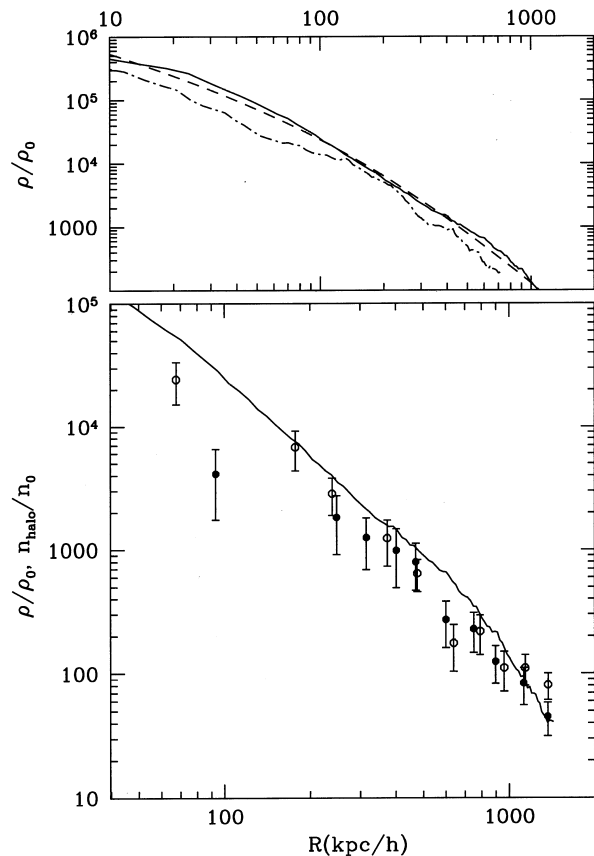


FIG. 3.—Density profile of the cluster shown in Figs. 1 and 2. *Top panel*: DM density in units of the mean matter density at $z = 0$ (solid line) and at $z = 1$ (dot-dashed line); the dashed line shows the NFW fit to the $z = 0$ density profile. The $z = 1$ density profile is given in proper units: the radius is given in proper scale, and the mean matter density is estimated at $z = 0$. *Bottom panel*: Number density profiles of halos in the cluster at $z = 0$ (solid circles) and at $z = 1$ (open circles) as compared with the $z = 0$ density profile of DM (solid curve). The error bars show 1σ Poisson errors. Halos with more than 30 bound particles and with maximum circular velocity larger than 100 km s^{-1} at $z = 0$ and larger than 120 km s^{-1} at $z = 1$ were used to estimate the average density n_0 (see § 4.3 for details). The profile at $z = 1$ is rescaled into proper units similar to that of the DM in the top panel.

also shown that a mass resolution of $\approx 10^9 h^{-1} M_{\odot}$ is sufficient, provided that force resolution is high. Two runs with a force resolution of $3 h^{-1}$ kpc and with mass resolutions of 10^8 and $10^9 h^{-1} M_{\odot}$ resulted in identical mass evolution. It is worth noting that in these experiments the halo was followed until it was totally destroyed by the tidal field ($\gtrsim 5$ Gyr in most cases). In real simulations, however, clusters form only at $z \lesssim 1$ and most of the accreted halos spend $\lesssim 5$ Gyr in clusters. During this time halos lose 80%–90% (depending on the orbit) of their initial mass. Thus, if the mass resolution is $\approx 10^9 h^{-1} M_{\odot}$, the halos with initial mass $\gtrsim 10^{11} h^{-1} M_{\odot}$ can be identified even after spending a substantial time in a cluster.

Details of the evolution of halos in clusters depend sensitively on the parameters of the halo orbit. Specifically, the mass-loss rate depends on the pericenter and on the eccentricity of the orbit. A halo on a very eccentric orbit survives for a considerably longer time than a halo on a circular orbit, even if the radius of the latter is larger than the pericenter. For example, a halo on a circular orbit with a radius of $250 h^{-1}$ kpc was totally destroyed in less than 5 Gyr, while a halo on a very eccentric orbit with the pericenter of

only $125 h^{-1}$ kpc survived for more than 10 Gyr. The explanation for this is simple: a halo on a circular orbit spends all of its time in a high-density cluster core suffering a steady mass loss, while a halo on the eccentric orbit spends only a small fraction of its orbital period in the core.

With the resolution quoted above, only a relatively small fraction of halos can be tidally destroyed in clusters. Only the halos with the apocenter $\lesssim 300 h^{-1}$ kpc are subject to the destruction. It can be expected that halos which are accreted when the cluster was young and its radius was small ($\sim 300\text{--}500 h^{-1}$ kpc) have small apocenters. The fraction of such halos in a $z = 0$ cluster is small. Our estimates show that for halos with large apocenters the dynamical friction cannot bring the apocenter considerably closer to the cluster center. The tidal stripping reduces the halo mass very efficiently, thus increasing the friction time.

The tidal stripping that halos suffer in clusters has an important effect on their density profiles. It appears that the halo profile is affected at all radii and not only at radii close to the tidal radius. Indeed, the trajectories of particles in a halo are mostly eccentric and after a crossing time the absence of the stripped particles will be “felt” by the whole halo. The change in the density profile means, of course, a change in the maximum circular velocity of the halo. The effect is not dramatic because the fraction of particles on highly eccentric orbits is rather small and the central regions of halos are thus affected the least. Typically, the circular velocity of the halos is reduced during their evolution in the cluster by 20%–30%. This correction was taken into account in Figure 3 by reducing the velocity cut from 120 km s^{-1} at $z = 1.0$ to 100 km s^{-1} at $z = 0.0$.

The tidal destruction is important only for cluster-size halos (where tidal fields are the strongest). There are three massive clusters in our ΛCDM_{60} simulation with mass $\gtrsim 2 \times 10^{14} h^{-1} M_{\odot}$. There is one “Coma cluster” with velocity dispersion $\sigma_{3D} = 1654 \text{ km s}^{-1}$ and mass $M = 6.4 \times 10^{14} h^{-1} M_{\odot}$ inside $1.43 h^{-1}$ Mpc radius. The cluster contains 201 halos of mass greater than $3 \times 10^{10} h^{-1} M_{\odot}$ inside a $2 h^{-1}$ Mpc box and nine halos inside $0.3 h^{-1}$ Mpc. Unfortunately, the cluster has suffered a recent major merger, and it was difficult to study the radial distribution of halos. One of the other two clusters also shows an indication of an ongoing merger. It has two subclusters in the central region separated by $\approx 0.5 h^{-1}$ Mpc. Therefore, we will focus on the third cluster which has a relatively regular appearance (see Fig. 1).

The cluster contains 121 bound halos with $\gtrsim 20$ particles inside $1.5 h^{-1}$ Mpc. There are 231,200 DM particles inside the virial radius of $1.28 h^{-1}$ Mpc. The virial mass of the cluster has increased from $M_{\text{vir}} = 7.9 \times 10^{13} h^{-1} M_{\odot}$ at $z = 1$ to $M_{\text{vir}} = 2.4 \times 10^{14} h^{-1} M_{\odot}$ at $z = 0$. Figure 3 shows the density profile of matter and the radial number density profile of DM halos inside the cluster. The DM density profile at $z = 0$ is well approximated by the NFW profile. For comparison, we also present the density profile of this cluster at redshift 1. Note that at $z = 1$ the radius is given in proper units and the mean matter density (ρ_0) is estimated at $z = 0$. Similarly, the bottom panel of Figure 3 shows the number density profile of halos in the cluster at $z = 0$ and at $z = 1$. Halos with more than 30 bound particles and with limits on the maximum circular velocity $V_{\text{max}} \geq 100 \text{ km s}^{-1}$ and $V_{\text{max}} \geq 120 \text{ km s}^{-1}$ (the change is for the reasons explained above) for $z = 0$ and $z = 1$, respectively, were used. The mean number density of halos, n_0 ,

was estimated using all halos in the simulation within the above velocity limits ($N_h = 7628$ at $z = 0$). The profile at $z = 1$ is also rescaled into proper units. Figure 3 clearly indicates that the number of halos in the central $300 h^{-1}$ kpc (proper radius) has declined substantially from $z = 1$ to the present epoch. In the central $300 h^{-1}$ kpc there are 3 times as many halos (24) at $z = 1.0$ than at $z = 0$. If we interpret the difference as due to tidal destruction, then 16 halos were destroyed in the central part. The situation is different at larger radii: there are 57 and 50 halos at $0.3 h^{-1}$ Mpc $< r < 1.3 h^{-1}$ Mpc for $z = 1$ and $z = 0$, respectively. Note, that we compare the number of halos in the same proper volume at these two moments: the volume corresponding to the virial radius of the cluster at $z = 0$ (the virial radius at $z = 1$ is smaller). The number density profile is thus virtually unaffected at $r \gtrsim 300 h^{-1}$ kpc.

5. RESULTS

In this section we will present results on the evolution of the two-point correlation function and bias (as defined by eq. [1]) in the simulations described in the previous section. The presentation of the results is split into two subsections. In § 5.2 we present the results of our largest simulation: ΛCDM_{60} . In § 5.3 we present the results of the rest of our simulations of different cosmological models. Thus, we will first focus on the results of the most realistic of the studied models, ΛCDM (see § 3), and then will discuss the differences between cosmological models. However, before we proceed with the presentation of the results, we will first compare our estimate of the DM correlation function with estimates which have been performed by different authors and with different numerical codes.

5.1. The DM Correlation Function in the ΛCDM Studies: Comparison with Other Studies

In Figure 4 we compare the two-point correlation function of the DM in the ΛCDM model (the ART run ΛCDM_{60}) with similar estimates presented by Klypin et al. (1996) and by Jenkins et al. (1998). The two latter estimates were done with different codes (PM in Klypin et al. and AP³M in Jenkins et al.) and different resolutions (cell size of $62 h^{-1}$ kpc for the PM and $30 h^{-1}$ kpc [Plummer] for the AP³M). All simulations followed 256^3 particles, although physical mass resolution was different because of the different box sizes (50, 60, and $141.3 h^{-1}$ Mpc for the PM, ART, and AP³M simulations). Although the cosmological model was exactly the same in all three estimates,¹⁵ the normalization of the power spectrum was slightly different. The rms mass fluctuations on a scale of $8 h^{-1}$ Mpc σ_8 was 0.9, 1.0, and 1.1 for the AP³M, ART, and PM simulations, respectively. Therefore, we have multiplied (divided) the DM correlation function of AP³M (PM) simulation by 1.1^2 in order to account for the differences in normalization. Figure 4 indicates that there is a very good agreement between all estimates at scales $\approx (0.2\text{--}2) h^{-1}$ Mpc. The ART and AP³M estimates agree to better than 10% at scales of $0.03\text{--}7 h^{-1}$ Mpc! On larger scales the ART correlation function has a smaller amplitude than that of the AP³M because of the factor of 2.35 smaller box size of the former. This result is in an agreement with previous studies (e.g.,

¹⁵ Note, however, that there are small differences in the approximation used for the power spectrum between the simulations.

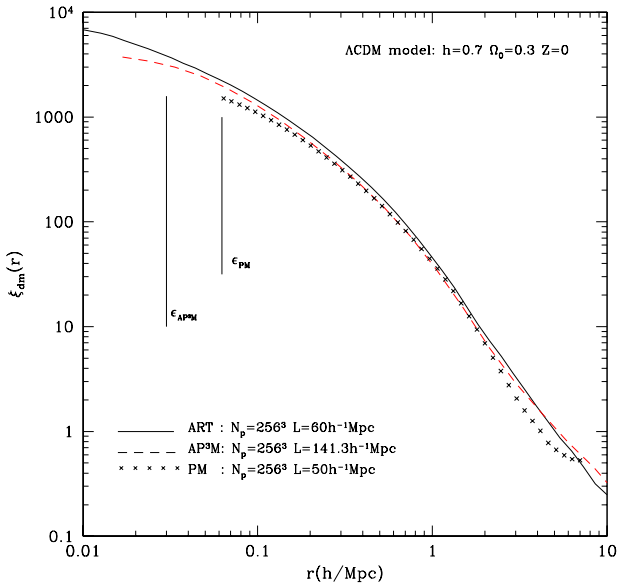


FIG. 4.—Comparison of the correlation functions of the DM ξ_{dm} in the ΛCDM model estimated by different authors with different numerical resolutions and codes. The solid curve shows ξ_{dm} in our ΛCDM_{60} run, simulated using the ART code. The dashed curve shows ξ_{dm} estimated by Jenkins et al. (1998) using the AP³M code. The crosses show ξ_{dm} estimated by Klypin et al. (1996) using the PM code. The AP³M and PM correlation functions were rescaled as described in § 5.1 to account for the difference in normalization between different simulations. All simulations followed evolution of 256^3 particles. The vertical lines indicate formal force resolution for each code (the line for the ART code at $1.8 h^{-1}$ kpc is off the plot).

Colín, Carlberg, & Couchman 1997 and references therein) which concluded that the correlation function is underestimated at scales of $\gtrsim 0.1$ of the simulation box size. Nevertheless, the agreement is striking at smaller scales, given all the differences (including cosmic variance) between the estimates. We conclude, therefore, that the correlation functions presented in the next subsection are robust at scales of $\lesssim 7 h^{-1}$ Mpc. This scale is, of course, lower ($\approx 3\text{--}4 h^{-1}$ Mpc) for the $30 h^{-1}$ Mpc simulations presented in § 5.3.

5.2. Evolution of the Correlation Function and Bias in the ΛCDM Model

In Figure 5 we plot the evolution of the correlation function of both the DM ξ_{dm} and the DM halos ξ_{hh} in our ΛCDM_{60} simulation. All results in this and the following sections are presented in comoving coordinates. The halo-halo correlation function was constructed using halos with $V_{\text{max}} \geq 120 \text{ km s}^{-1}$. Note that although the earliest moment at which we show the correlation function is $z = 5$, the first halos in this simulation collapsed at redshift $z \approx 10$ and hundreds of halos are identified at $z \approx 7\text{--}8$. The number of halos in the $V_{\text{max}} \geq 120 \text{ km s}^{-1}$ catalog is approximately 4300, 10,000, and 7500 for redshifts of 5, 2, and 0, respectively. The good statistics result in a very accurate estimate of the correlation function. The number of pairs per scale bin used to estimate ξ_{hh} is greater than 50 in all cases. Typically, 60–150 for $r < 0.2 h^{-1}$ Mpc, 200–1000 for $0.2 h^{-1} \text{ Mpc} < r < 1 h^{-1} \text{ Mpc}$, and greater than 1000 for the larger scales. The pure Poisson errors associated with each of the points are thus negligibly small, except for the first 2–3 bins (where Poisson errors are still small:

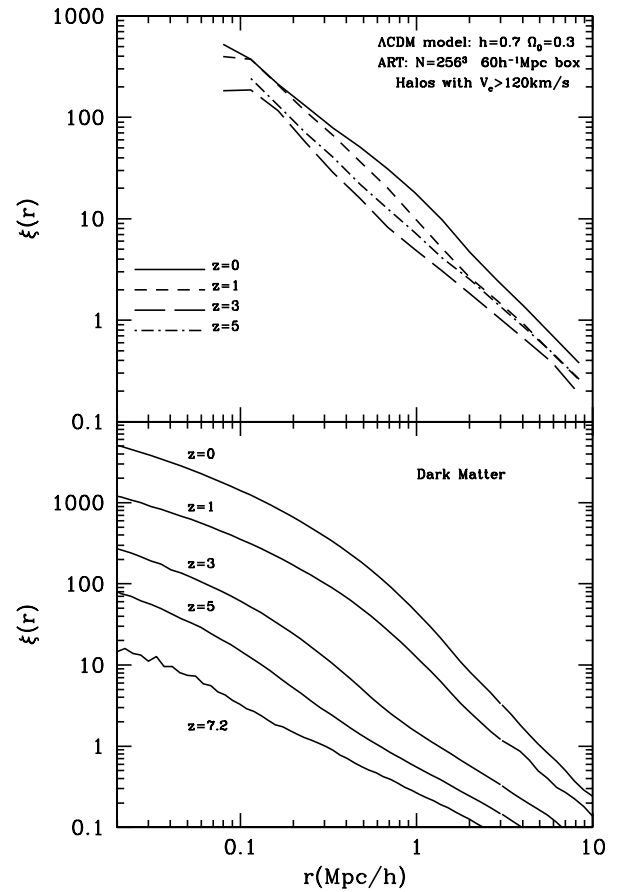


FIG. 5.—Evolution of the two-point correlation function of the DM (*bottom panel*) and halos (*top panel*) in the ΛCDM_{60} simulation. Only halos with maximum circular velocity greater than 120 km s^{-1} were used to estimate the halo correlation functions. Poisson errors for the halo correlation functions are negligible at scales $\gtrsim 0.2 h^{-1}$ Mpc and are not shown for clarity; at scales less than $0.2 h^{-1}$ Mpc the error bars are $\lesssim 20\%$ (see § 5.2 for details). The best-fit parameters of the power-law fit to the halo correlation functions are given in Table 4.

$\lesssim 20\%$). There are subtler errors associated with radial binning, but these are also less than a few percent.

Figure 5 shows that the shapes of the matter and halo-halo correlation functions are quite different. The matter correlation function changes its shape from almost a power law to a complicated shape. The slope of ξ_{dm} at scales $\lesssim 0.5 h^{-1}$ Mpc stays approximately constant throughout the evolution, while at the larger scales ξ_{dm} significantly steepens. The amplitude of the DM correlation function increases from $z = 5$ to $z = 0$ by factors of ≈ 60 and ≈ 10 at small and large scales, respectively. The halo-halo correlation function behaves very differently. Its shape can be well described by a power law at all epochs. The amplitude of ξ_{hh} evolves nonmonotonically: it decreases somewhat from $z = 5$ to $z = 3$ and then gradually increases. The evolution, however, is much more modest than the dramatic evolution of the ξ_{dm} : the maximum difference in amplitude among any two epochs is only a factor of 2. The details of the ξ_{hh} evolution are illustrated in Figure 6. This figure shows the evolution of the ξ_{hh} amplitude at a variety of different comoving scales (indicated on the right) for the three ΛCDM runs from our set of simulations (see Table 2). Different initial conditions of these runs allow us to evalu-

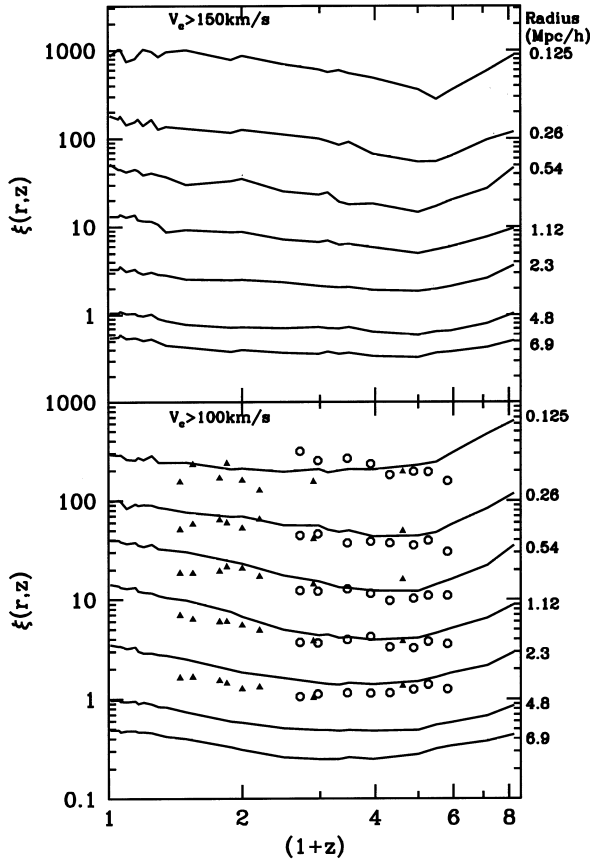


FIG. 6.—Evolution of the correlation function of halos in ΛCDM_{60} simulation at various comoving scales. Each curve shows the amplitude of the correlation function at a fixed comoving radius indicated on the right side of the panels. The correlation functions were estimated for halos with circular velocity greater than 150 km s^{-1} (top panel) and greater than 100 km s^{-1} (bottom panel). The solid curves and open circles indicate amplitudes in the ART 60 and $30 h^{-1}$ Mpc simulations, respectively; the triangles show the amplitude in the $30 h^{-1}$ Mpc AP³M simulation (see § 5.2 for details and discussion).

ate the cosmic variance, while different particle masses and spatial resolutions (by a factor of 8 and 2, respectively) of ΛCDM_{60} and $\Lambda\text{CDM}_{30}^{\text{ART}}$ allow us to check for the resolution effects. Comparison of $\xi_{\text{hh}}(r, z)$ in the $30 h^{-1}$ Mpc runs simulated with different codes and with significantly different resolutions shows that the two runs agree very

well. The $\Lambda\text{CDM}_{30}^{\text{ART}}$ simulation had the best mass and force resolution, yet we do not find any visible systematic differences at scales $\lesssim 2 h^{-1}$ Mpc with the other two simulations. There is an indication that at $r \gtrsim 2 h^{-1}$ Mpc the amplitude in the $30 h^{-1}$ Mpc simulations is systematically lower than that in the ΛCDM_{60} , which can be explained by the effects of finite box size. This is in agreement with the expectation that the finite-size effects become important at scales $\gtrsim 3 h^{-1}$ Mpc (≈ 0.1 of the box size). At smaller scales, where we expect the $30 h^{-1}$ Mpc simulations to produce correct results, the agreement is very good.¹⁶ Besides the illustration of a very mild evolution of ξ_{hh} , Figure 6 also shows that there is a common feature of the evolution. Although the exact evolution depends to some extent on the scale, the amplitudes at all scales are quite high (as high or higher as they are at $z = 0$) at very high redshift ($z \approx 7$). The amplitude then decreases until $z \sim 2-4$ and grows steadily at lower redshifts. It is important to note that this evolution is more complicated than the simple evolution models often used in the observational and theoretical analyses: $\xi(r, z) = (r/r_0)^{-\gamma}(1+z)^{-(3-\gamma+\epsilon)}$. Figure 6 shows that parameter ϵ estimated by such analyses would depend not only on the redshift range used, but also on the scale at which the amplitude is measured (as well as on other parameters such as the object's mass). This calls into question the usefulness of such a simplistic approach (see also arguments in Moscardini et al. 1998). Note that there is also some observational evidence (Giavalisco et al. 1998) indicating that the above parameterization is a poor description of the observed galaxy clustering evolution. For a limited range of redshifts $z \sim 0-1$, we find only very weak evolution of halo clustering in comoving coordinates indicating a value of $\epsilon \approx -1$. This value seems to be favored by observations of galaxy clustering at these redshifts (e.g., Postman et al. 1998).

The power-law fits to ξ_{hh} of the form $\xi_{\text{hh}}(r) = (r/r_0)^{-\gamma}$ for various epochs and for halo catalogs with different cuts in the maximum circular velocity are presented in Table 4. Direct (rather than linear fits to $\lg \xi_{\text{hh}} - \lg r$) weighted power-law fits were done to ξ_{hh} with the Levenberg-Marquardt method described by Press et al. (1992). Each bin of the correlation function was weighted with its Poisson error $\sigma_{\xi} = (\xi_{\text{hh}} + 1)/(n_p)^{1/2}$, where n_p is the number of halo pairs in the bin. Visual inspection shows that power-

¹⁶ Note that some cosmic variance is expected for these box sizes.

TABLE 4
POWER-LAW FITS TO ξ_{hh} IN THE ΛCDM_{60} SIMULATION^a

| z | $V_{\text{max}} > 120 \text{ km s}^{-1}$ | | $V_{\text{max}} > 150 \text{ km s}^{-1}$ | | $V_{\text{max}} > 200 \text{ km s}^{-1}$ | |
|----------|--|-------------------|--|-------------------|--|-------------------|
| | r_0 | γ | r_0 | γ | r_0 | γ |
| 0.0..... | 4.864 ± 0.011 | 1.704 ± 0.004 | 4.789 ± 0.024 | 1.687 ± 0.009 | 5.082 ± 0.062 | 1.650 ± 0.022 |
| 0.5..... | 4.145 ± 0.009 | 1.684 ± 0.004 | 4.040 ± 0.019 | 1.726 ± 0.009 | 4.534 ± 0.049 | 1.777 ± 0.020 |
| 1.0..... | 3.760 ± 0.007 | 1.694 ± 0.003 | 3.944 ± 0.015 | 1.762 ± 0.007 | 4.387 ± 0.038 | 1.869 ± 0.016 |
| 1.5..... | 3.419 ± 0.006 | 1.642 ± 0.003 | 3.823 ± 0.013 | 1.715 ± 0.006 | 4.288 ± 0.035 | 1.831 ± 0.016 |
| 2.0..... | 3.103 ± 0.006 | 1.588 ± 0.003 | 3.831 ± 0.011 | 1.629 ± 0.006 | 4.375 ± 0.036 | 1.702 ± 0.016 |
| 3.0..... | 2.974 ± 0.006 | 1.527 ± 0.004 | 3.453 ± 0.011 | 1.536 ± 0.006 | 4.327 ± 0.037 | 1.683 ± 0.016 |
| 4.0..... | 3.206 ± 0.009 | 1.516 ± 0.005 | 3.356 ± 0.011 | 1.498 ± 0.006 | 4.733 ± 0.044 | 1.598 ± 0.017 |
| 5.0..... | 3.602 ± 0.013 | 1.534 ± 0.007 | 3.661 ± 0.016 | 1.516 ± 0.008 | 4.829 ± 0.053 | 1.578 ± 0.020 |

^a Column description: z is redshift; r_0 and γ are the best-fit parameters of the power-law $\xi_{\text{hh}}(r) = (r/r_0)^{-\gamma}$ fit to the comoving halo-halo correlation function; comoving r_0 in units of h^{-1} Mpc.

law fits are very successful at scales $\gtrsim 0.3 h^{-1}$ Mpc, while at smaller scales there are $\approx 20\%$ – 30% deviations in some cases. The goodness of the fits is represented in rather small formal errors of the best-fit parameters r_0 and γ . We have estimated how these parameters change if the correlation function is rebinned differently and found that the change is always $\lesssim 3\%$. The examination of Table 4 shows that typical ranges of r_0 and γ are $\approx 3\text{--}5 h^{-1}$ Mpc and $\approx 1.5\text{--}1.7$, respectively. For all halo catalogs, parameters evolve slowly with redshift. The correlation length r_0 decreases somewhat between redshifts of 5 and 3 and then increases steadily until $z = 0$. The evolution of γ is even slower, with the tendency for γ to increase by $\approx 10\%$ from $z = 5$ to the present epoch. An important and interesting point is that the correlation amplitude, and hence the value of r_0 , is quite different for halo catalogs with different V_{\max} cuts. The correlation lengths for the $V_{\max} \geq 120 \text{ km s}^{-1}$ and $V_{\max} \geq 200 \text{ km s}^{-1}$ catalogs differ by 25% at $z \gtrsim 3$, while the difference is only $\approx 4\%$ at $z = 0$. This means that there is a mass segregation of halo-clustering properties at high redshift, which, however, is erased during the subsequent evolution.

During the last few years there has been tremendous progress in the observational studies of high-redshift galaxy clustering. We will discuss how our results on the halo clustering evolution compare with the results of observations in § 6. Here, however, we present a comparison of the ξ_{hh} with the most accurate measurement of the galaxy correlation function ξ_{gg} (at $z \approx 0$) made using the APM galaxy survey (Baugh 1996). Figure 7 shows the $z = 0$ correlation functions of halos and DM in the Λ CDM model and the real space APM galaxy correlation function. The halo-halo correlation function was estimated for halo catalogs with cuts in the maximum circular velocity of 120, 150, and 200 km s^{-1} . The figure shows striking agreement between the halo and galaxy correlation functions: at scales $\gtrsim 0.3 h^{-1}$ Mpc the correlation functions of all halo catalogs match both the shape and the amplitude of the ξ_{gg} . The correlation function for the $V_{\max} > 150 \text{ km s}^{-1}$ catalog agrees with APM ξ_{gg} within errors at all probed scales. As we noted above, the differences that exist between the catalogs at high redshifts virtually vanish during the course of the evolution. This is manifested in the similarity of ξ_{hh} for different catalogs on scales $\gtrsim 0.3 h^{-1}$ Mpc. Note, however, that this does not mean that ξ_{hh} has no mass dependency. Rather, the result means that by $z = 0$ any mass dependency of the correlation function vanishes when averaged over a range of galactic masses. As was explained above, the Poisson errors of the halo correlation functions shown in Figure 7 are very small and were not shown for clarity. The robustness of the result can be estimated, however, by comparing the ξ_{hh} of the $V_{\max} > 120 \text{ km s}^{-1}$ and $V_{\max} > 150 \text{ km s}^{-1}$ catalogs. The number of halos in these catalogs is significantly different: 4708 and 2480, respectively. This makes the halo samples largely independent. The correlation functions agree, however, within the Poisson errors.

While the correlation function of halos matches that of galaxies very accurately, the correlation function of matter ξ_{dm} matches ξ_{gg} neither in shape nor in amplitude.¹⁷ The amplitude is matched only at scales $\gtrsim 4\text{--}5 h^{-1}$ Mpc. At

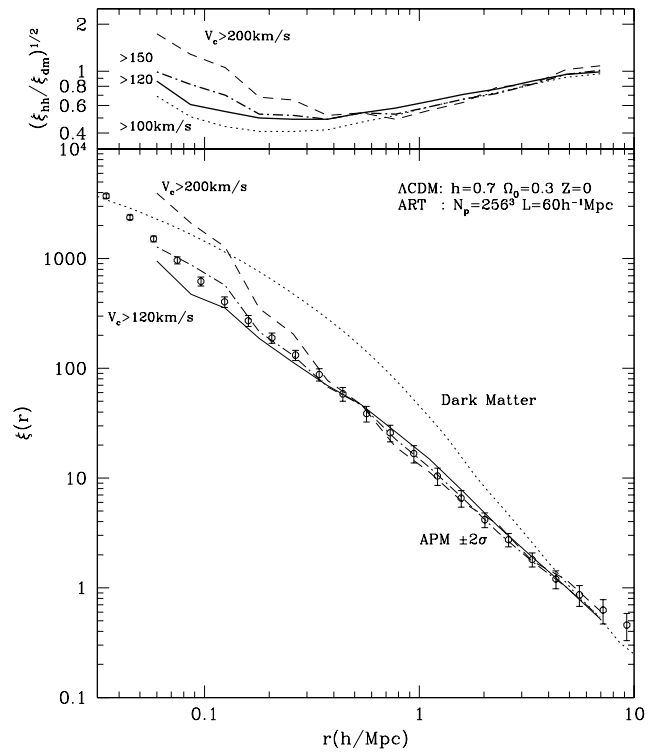


FIG. 7.—*Bottom panel*: Comparison of the halo correlation function in the Λ CDM₆₀ simulation with the correlation function of the APM galaxies (Baugh 1996). Results for halos with maximum circular velocity larger than 120, 150, and 200 km s^{-1} are presented by the solid, dot-dashed, and dashed curves, respectively. The dotted curve shows the DM correlation function. Note that at scales $\gtrsim 0.3 h^{-1}$ Mpc the halo correlation function does not depend on the limit in the maximum circular velocity (see § 5.2 for details). *Top panel*: Dependence of bias on scale and maximum circular velocity. The curve labeling is the same as in the bottom panel, except that the dotted line now represents the bias of halos with $V_{\max} > 100 \text{ km s}^{-1}$.

smaller scales it is much higher than the amplitude of the APM ξ_{gg} , implying that DM halos are antibiased at these scales with respect to the DM. Moreover, the difference in shape between ξ_{hh} and ξ_{dm} implies that the bias is scale dependent. The scale dependence of the bias $[\{[\xi_{\text{hh}}(r)/\xi_{\text{dm}}(r)]^{1/2}\}]$ for the halo correlation functions is shown in the top panel of Figure 7. The bias varies significantly at scales $\lesssim 5 h^{-1}$ Mpc in the range $\sim 0.5\text{--}1$. Moreover, as was shown in Figure 5, the shape of the correlation function of DM differs from that of ξ_{hh} at all epochs and evolves much more strongly than the correlation function of halos. The former fact implies that the bias is scale dependent at all epochs, while the latter means that the bias evolves rapidly with cosmic time. The evolution of bias in the Λ CDM₆₀ run is illustrated in Figure 8. The evolution is shown for different halo catalogs and at different scales. The bias evolves very rapidly from the value of $\sim 3\text{--}5$ at $z \approx 5$ to $\sim 0.5\text{--}1$ at $z = 0$. The evolution depends on the velocity (or mass) cut of the catalog at high z : the halos in the catalogs with higher velocity cuts exhibit stronger clustering. This difference vanishes, however, at $z \lesssim 0.5$. The evolution of the scale dependence of the bias is also interesting. At high redshifts the bias was larger at small scales. At small redshifts the halos are almost unbiased ($b \approx 1$) on a few-megaparsec scales and are antibiased ($b \approx 0.5\text{--}0.6$) on small scales.

¹⁷ This result is in agreement with conclusions of Jenkins et al. (1998). As was shown in the previous section, our ξ_{dm} agrees very well with that calculated by Jenkins et al.

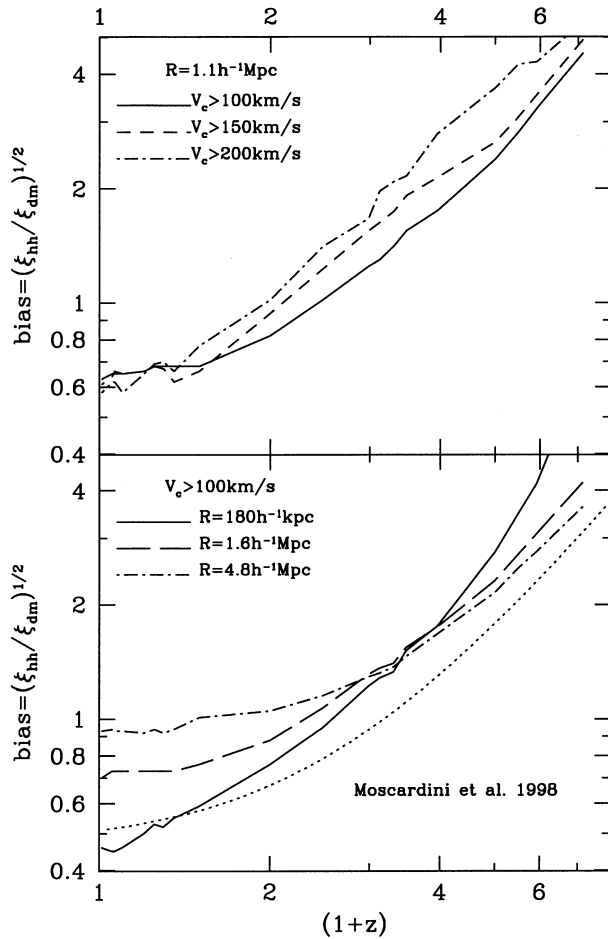


FIG. 8.—*Top panel*: The evolution of bias at a comoving scale of $0.54 h^{-1} \text{ Mpc}$ for halos with a different lower limit on the maximum circular velocity in the ΛCDM_{60} simulation. *Bottom panel*: Dependence of the bias on (comoving) scale for halos with maximum circular velocity greater than 100 km s^{-1} .

5.3. Evolution of the Correlation Function and Bias in Different Cosmological Models

Is the evolution of bias observed in the ΛCDM simulations specific to this model or is this evolution similar for all of the models? We address this question by comparing results presented in the previous section with results of the $30 h^{-1} \text{ Mpc}$ simulations of other cosmological models (see Table 2). Figures 9–12 show the correlation functions of halos ξ_{hh} and the DM ξ_{dm} for the four AP³M $30 h^{-1} \text{ Mpc}$ runs at four epochs. Halos with $V_{\text{max}} > 200 \text{ km s}^{-1}$ were used to compute $\xi_{\text{hh}}(r, z)$ for the SCDM and the τCDM models. A lower $V_{\text{max}} > 120 \text{ km s}^{-1}$ limit was used for the OCDM and ΛCDM_{30} models. The difference in the V_{max} limits is explained by the difference in the matter density Ω_0 that results in a different mass resolution of the simulations. In the OCDM and the ΛCDM_{30} runs halos with $V_{\text{max}} > 200 \text{ km s}^{-1}$ are scarce, while the poorer mass resolution does not allow us to reduce the limit to 120 km s^{-1} in the SCDM or the τCDM runs. The total number of halos found in the simulations is indicated in each panel. The number depends on the epoch and model and varies from a maximum of 1942 (in the SCDM run at $z = 1.9$) to a minimum of 611 (in the τCDM run at $z = 3.6$). The statistics of halos are poorer than in the ΛCDM_{60} simulation. There-

fore, we plot the error bars associated with each point of ξ_{hh} . We estimate both Poisson and bootstrap error bars and plot the largest of the two. The bootstrap error bars have been estimated as follows. For each run and each epoch we have drawn five randomly selected samples of halos from the corresponding halo population. The number of halos in each sample is one half of the total. We then compute the rms fluctuation between the samples and divide it by $2^{1/2}$ to get the 1σ error bar.

Figures 9–12 show that in all models the evolution of the correlation function is qualitatively similar to that observed in the ΛCDM model. For example, the shape of the ξ_{hh} is similar (power law) in all models and is always different from the corresponding ξ_{dm} . This means that the scale-dependent bias is universal in cosmological models. Details of the evolution are, however, model dependent. The most drastic differences are seen at the highest redshifts. The figures, for example, clearly show that the bias at $z = 3.4$ has very different values in different models. While bias in the two low- Ω_0 models is very similar, the distribution of halos at this redshift is only weakly biased in the SCDM model, as opposed to the strongly biased distribution in the τCDM model. The evolution of the halo correlation function at three different comoving scales ($0.3, 1,$ and $3 h^{-1} \text{ Mpc}$) for all models is plotted in Figure 13. The solid lines in both panels represent results for the ΛCDM model with the ART code in the $60 h^{-1} \text{ Mpc}$ box. In the upper panel the evolution is shown for the halo catalogs with a fixed number density of halos, which was achieved by varying the V_{max} limit in different models. Note that in this case we compare correlations of halo samples with different mass functions: the ΛCDM and OCDM halo samples contain many low-mass halos, while samples in the $\Omega_0 = 1$ models contain only massive halos. Such comparison is interesting for comparisons with observations when we know the number density of objects in the sample rather than their mass (or type). At scales $\lesssim 1 h^{-1} \text{ Mpc}$, differences between the models are not significant. At $3 h^{-1} \text{ Mpc}$ and at high z the amplitude of ξ_{hh} in the SCDM model is significantly lower than in other models. The amplitude in the rest of the models is surprisingly similar. Therefore, if the biased galaxy formation scenario is correct and galaxies can be associated with host halos, this result may have interesting implications for the interpretation of clustering observations. To be able to differentiate between the models, we must know what type of the objects was used to estimate the clustering signal. The knowledge of the number density of objects in the sample is not sufficient. The point is to some extent illustrated by the lower panel of Figure 13, where we compare the evolution of the ξ_{hh} amplitude in ΛCDM_{60} , SCDM, and τCDM models for the halo catalogs with the same selection criterion ($V_{\text{max}} > 200 \text{ km s}^{-1}$). It is obvious that in this case the differences between the models are significant. Although the differences are smaller at low redshifts, at $z \approx 3.5$ the difference in the amplitude between the ΛCDM and SCDM models is almost an order of magnitude. This difference can probably be explained by the delayed formation of galaxy-size halos in the ΛCDM model as compared with the SCDM model. The halos in the ΛCDM form at lower redshifts with high statistical bias, while halos in the SCDM systematically form earlier and thus have had time to go through merging evolution. The effect of the latter is to decrease the bias (e.g., Moscardini et al. 1998). Note also that merging rates are higher in $\Omega_0 = 1$

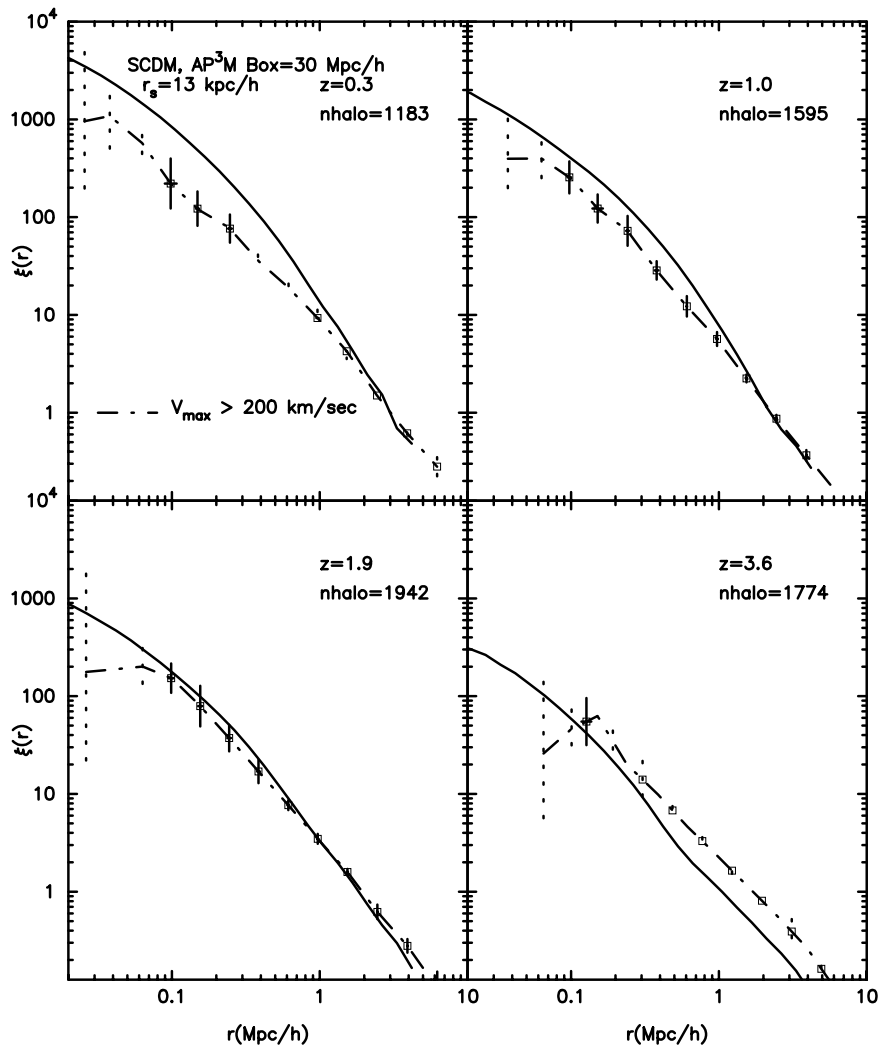


FIG. 9.—Evolution of the correlation function of the DM (*solid lines*) and halos (*dot-dashed line*) for the SCDM model in the $30 h^{-1}$ Mpc AP³M simulation. The panels show the correlation functions at different redshifts. Only halos with maximum circular velocity larger than 200 km s^{-1} were used to compute the halo correlation function. The number of halos used to estimate the correlation function is indicated in each panel. The Poisson errors (*dotted line*) and bootstrap errors (*solid line*) are shown by vertical bars (see § 5.3 for details).

models (e.g., Carlberg 1990). These results show that predictions of cosmological models are very different for samples of objects selected with the same set of criteria for all models.

The evolution of bias at scales 0.3 and $1 h^{-1}$ Mpc is shown in Figure 14 for all models. Here again we compute the halo correlation function for the fixed number density of halos. Evolution of bias in all models is qualitatively similar to that of the Λ CDM model discussed above: the bias is a very strong function of redshift. However, unlike the ξ_{hh} amplitude, the value of bias at these scales is very different among the models. This is not very surprising because when the number density of halos is fixed, different models have very similar amplitudes of ξ_{hh} (see Fig. 13) but very different amplitudes of ξ_{dm} . The latter is explained by the differences in the cosmological parameters, normalization, and the shape of the power spectrum. A more interesting implication of Figure 14 is that differences in bias get smaller at low redshifts, virtually disappearing at $z = 0$. The same effect can be observed in the evolution of the amplitude in Figure 13. As we will argue in the next section, the evolution of the

halo correlations and bias at these scales is likely to be driven by the halo dynamics within nonlinear structures, in which case the differences between different cosmologies are largely erased. The evolution shown in Figures 13 and 14 provides, therefore, indirect support for this point: the differences in clustering amplitude and bias between the models disappear at $z \lesssim 1$, where most of the clustering signal comes from the halos located in nonlinear structures.

To conclude, we note that while we did not find a significant difference in the present-day bias between cosmological models with a similar normalization ($\sigma_8 \approx 1$; see Table 1), there is a difference between bias in low- and high- σ_8 normalization for $\Omega_0 = 1$ models. The $z = 0$ bias in the $\sigma_8 = 0.5$ normalized SCDM model corresponds roughly to the bias in the $\sigma_8 = 1.0$ model at redshift $z \approx 1$. The additional difference, however, is caused by the different particle velocities at the rescaled redshift which affects properties of halos. We have rescaled the SCDM simulation and redone our analysis for the $\sigma_8 = 0.5$ normalization. The resulting evolution of bias is quite different from that in the $\sigma_8 = 1.0$ case (Fig. 9) and is similar to the evolution in the

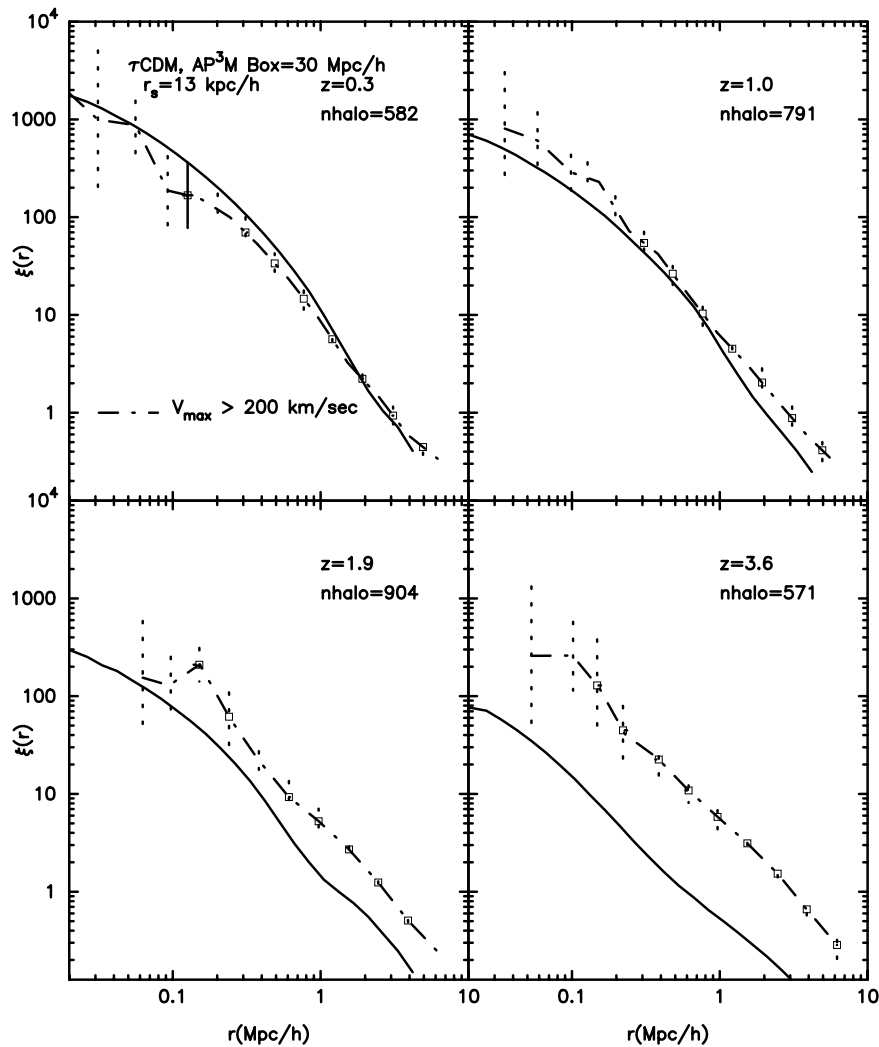


FIG. 10.—Same as Fig. 9, but for the τ CDM model. As in Fig. 9, only halos with $V_{\max} > 200 \text{ km s}^{-1}$ were used.

$\sigma_8 = 1.0$ τ CDM model (Fig. 10). The high-redshift bias in low- σ_8 CDM model is high [$b(z = 2.5) \approx 3-4$], and there is no statistically significant bias or antibias at $z = 0$.

6. DISCUSSION

It is interesting to compare the evolution of the halo correlation function and the bias observed in our simulations with predictions of the analytical models and results of previous numerical simulations. The fact that the clustering strength of halos at high redshifts is comparable to that at the present epoch has been noted in the results of many simulations (e.g., Davis et al. 1985; Brainerd & Villumsen 1994; Colín et al. 1997 and references therein). Bagla (1998) summarizes the generic behavior of the correlation amplitude of halos above a certain mass: the amplitude is high at very high redshifts, when halos are being formed, decreases thereafter and reaches a minimum, and then increases slowly and steadily until the present epoch. The results presented in § 5 (see Figs. 6 and 12) are in agreement with this picture. Thus, there seems to be good qualitative (although, in some cases, not quantitative) agreement among results of different numerical simulations concerning the evolution of the halo correlation function.

Analytical models have reached a sufficient degree of sophistication to be able to predict the evolution of halo

clustering in mildly nonlinear regimes (see § 2). The halos are found to form at the peaks of the density field (e.g., Frenk et al. 1988), and their bias exhibits a simple scaling relation with the height of these peaks (Kaiser 1984; Bardeen et al. 1986). At any given epoch the halo population represents a mix of halos formed at different redshifts: newly born or already evolved through merging. The evolution of the correlation of halos in such a hierarchical framework is described using the extended Press-Schechter formalism (MW). To compare predictions of the analytical models with our results, we will use the approximation to the evolution of the effective bias given by equation (4) (Moscardini et al. 1998). This approximation describes the evolution of bias of a sample of all halos above a certain mass. This is roughly equivalent to our definition of halo samples with a limiting maximum circular velocity. The prediction of this approximation is shown in Figure 8 with the dotted line, where we used $b_{\text{eff}}(0) = 0.51$ and $\beta = 1.90$ (see eq. [5]) appropriate for our Λ CDM model and for the mass limit of $M \geq 10^{11} h^{-1} M_{\odot}$ (Moscardini et al. 1998). The analytical model is expected to provide a good approximation at scales where $\xi_{\text{hh}} \lesssim 1$ (Mo et al. 1996), i.e., at $r \gtrsim 4-5 h^{-1} \text{ Mpc}$ (see Table 4). Therefore, the analytical prediction should be compared with the curve showing evolution of bias at $r = 4.8 h^{-1} \text{ Mpc}$.

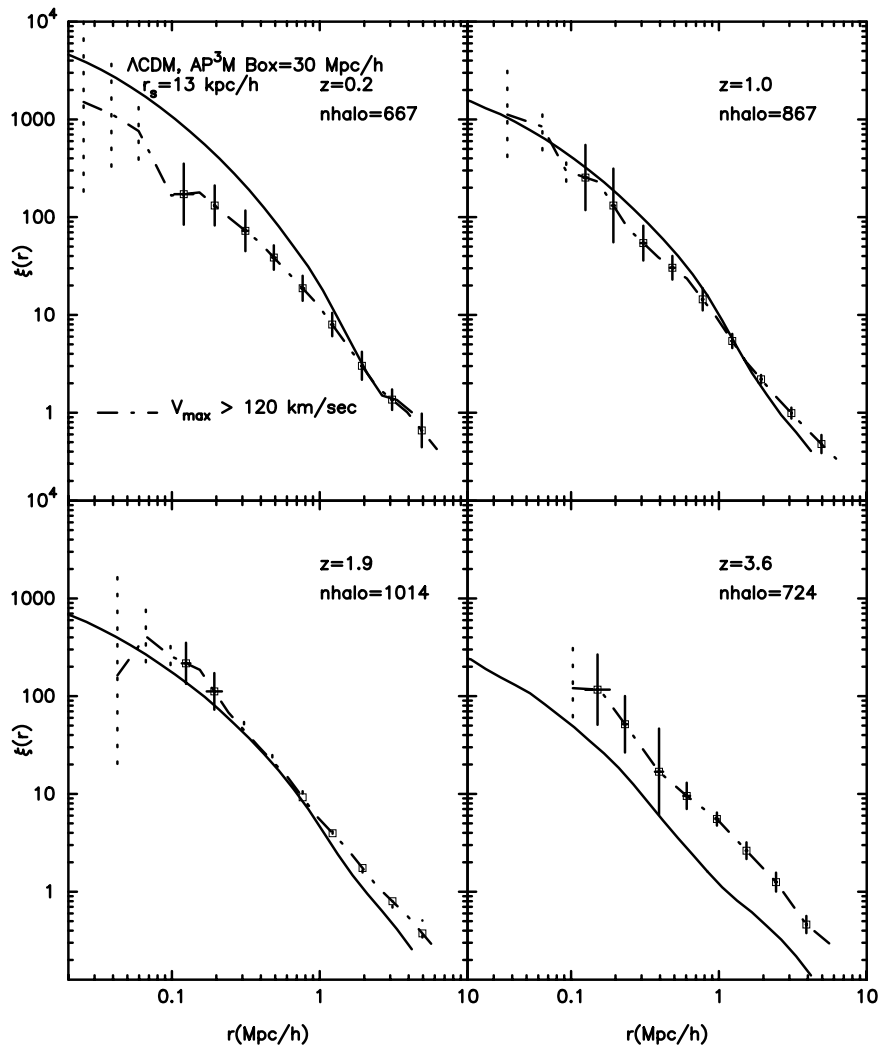


FIG. 11.—Same as Fig. 9, but for the Λ CDM model. Only halos with $V_{\max} > 120 \text{ km s}^{-1}$ were used to compute the correlation function (see § 5.3).

The comparison shows that both the numerical result and the analytical model predict a rapid decrease of bias with cosmic time. Moreover, at high redshifts ($z \gtrsim 3$) they agree well quantitatively. At lower redshifts, however, the two predictions deviate from each other and are different by a factor of 2 at $z = 0$. It is not clear what causes the difference in bias amplitude (see also Jing 1998). First, as we note in § 2, the mass weighting should not produce correct effective bias, if it is estimated from the correlation functions. However, we do not know how significant the expected differences should be. Second, there are significant differences in our definition of a halo from that of the Press-Schechter halo. The definition of the latter does not include “satellite” halos; a halo ceases to exist once it becomes bound to another halo (i.e., “merges”) and orbits inside that halo’s virial radius. Our definition, on the other hand, does take satellite halos into consideration, because we include in our halo list every gravitationally bound clump of particles, regardless of whether it is also bound to a larger system or not. The similarity between our numerical result and the prediction of the analytical model at $z \gtrsim 3$ may then be an indication that the two definitions are equivalent at these high redshifts. Indeed, large systems such as clusters and groups have not yet formed at these redshifts, and the fraction of satellite halos in our catalogs (i.e., all halos above a

certain mass limit) is relatively small. At smaller redshifts the ever larger fraction of halos become satellites to more massive halos and the two halo definitions result in rather different halo samples. This may explain the large difference predicted for the value of bias at $z = 0$. We have found that in our simulation the $z = 0$ amplitude of the two-point correlation function of the Press-Schechter halos (i.e., isolated in terms of their virial radius) at $r = 4.8 h^{-1} \text{ Mpc}$ is approximately 2 times as small as the amplitude of the correlation function of the BDM halos shown in Figure 7, resulting thus in the twice as small bias of $b \approx 0.5$.

We find also that the small-scale bias of the halo distribution is scale dependent regardless of the halo definition. The large-scale bias ($r \gtrsim 5 h^{-1} \text{ Mpc}$), on the other hand, is not probed in our simulations and may be independent of scale. This indeed was suggested by the simulations of Jing (1998). We think that the most encouraging result is the agreement between numerical and analytical modeling on the general form of the bias evolution demonstrated in Figure 8. This indicates that we now have a solid general understanding of the nature of bias and of the processes driving its evolution at redshifts $z \gtrsim 2-3$.

At smaller redshifts, the merging rate is considerably smaller and small-scale correlations are sensitive to the dynamics of halos inside the nonlinear structures. Particu-

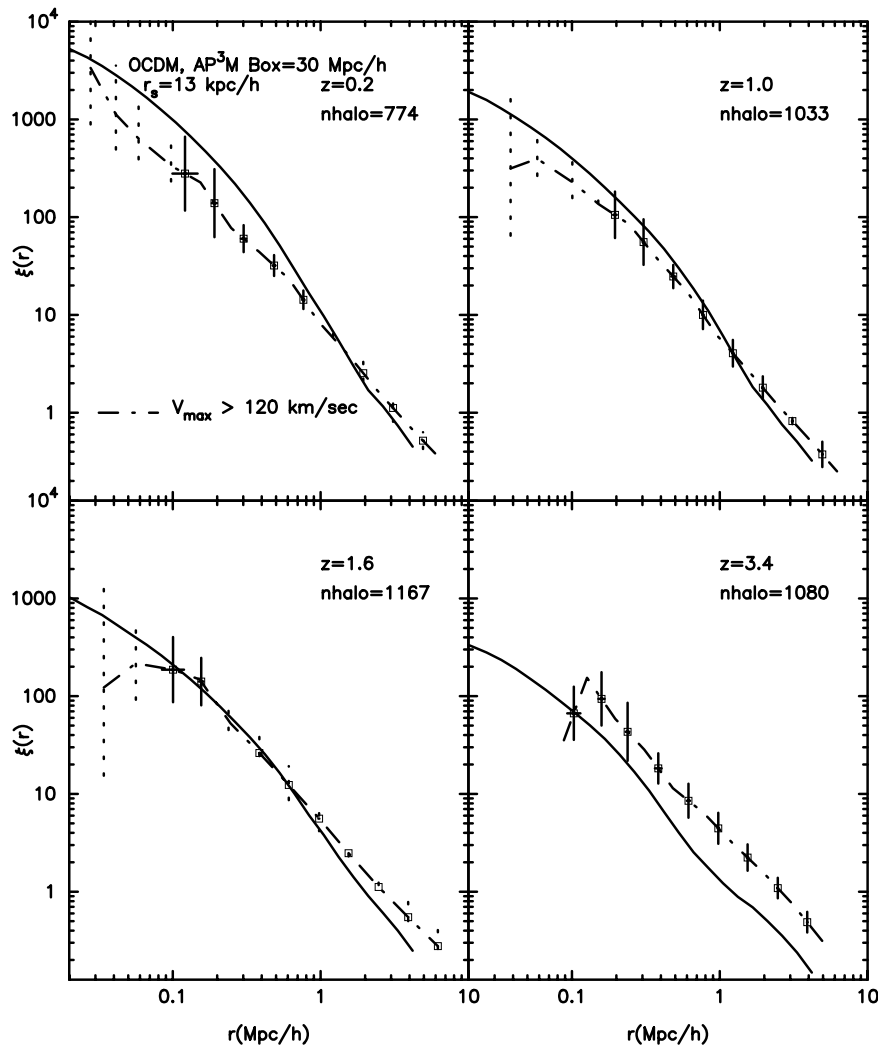


FIG. 12.—Same as Fig. 9, but for the OCDM model. As in Fig. 11, only halos with $V_{\max} > 120 \text{ km s}^{-1}$ were used (see § 5.3).

larly, the dynamics and the clustering evolution of satellite halos in high-density regions are essentially independent of the background cosmology and are driven by such processes as dynamical friction and tidal stripping (Kravtsov & Klypin 1999). These processes tend to suppress the growth of the correlation amplitude, thus counteracting the clustering growth due to the gravitational pull. This leads to the antibias observed in our simulations at nonlinear scales and at small redshifts. Indeed, the correlation amplitude at small scales ($r \lesssim 5 h^{-1} \text{ Mpc}$) is approximately constant at redshifts $z \approx 0-1$ (see Figs. 6 and 12). Moreover, antibias is observed in all cosmological models studied in this paper (see Figs. 9–12). The fact that differences in the correlation amplitude and bias, existing between the cosmological models at $z \approx 3$, virtually vanish by the present epoch (see Figs. 12 and 13) argues for the importance of the nonlinear halo dynamics. This result also implies that low-redshift clustering depends only weakly on the background cosmology. Therefore, the information about the underlying cosmological model can probably be extracted only from the high- z ($z \gtrsim 3$) clustering data. As was discussed in § 4.3, the numerical resolution required to assure the survival of halos in high-density regions is high and has not been reached in previous simulations. Our results therefore indi-

cate that high resolution is important for correct modeling of the bias evolution at small redshifts.

It would be very interesting to compare our results with the results of direct hydrodynamical simulations. Unfortunately, most of the recent hydro simulations that include additional physics relevant to galaxy formation either simulate considerably smaller boxes (Katz et al. 1999) or have a much poorer resolution (Blanton et al. 1999; Cen & Ostriker 1998). The former makes it difficult to compare correlation amplitudes and values of the bias (although qualitatively, Katz et al. 1999 report a very similar bias evolution to the one reported here). A poor resolution of a simulation inevitably leads to overmerging and therefore incorrect modeling of halo dynamics and evolution in high-density regions. This makes it difficult to make a meaningful comparison of the results, because as we explained above we believe that the dynamical processes significantly affect the bias evolution. The only simulation known to us that includes nonadiabatic gasdynamics and has a box size and resolution comparable to ours is a recent simulation by the Virgo Consortium (Jenkins et al. 1999). Preliminary comparisons indicate that our results on the galaxy correlation amplitude and its evolution are in good agreement with results of this simulation. The results of studies that

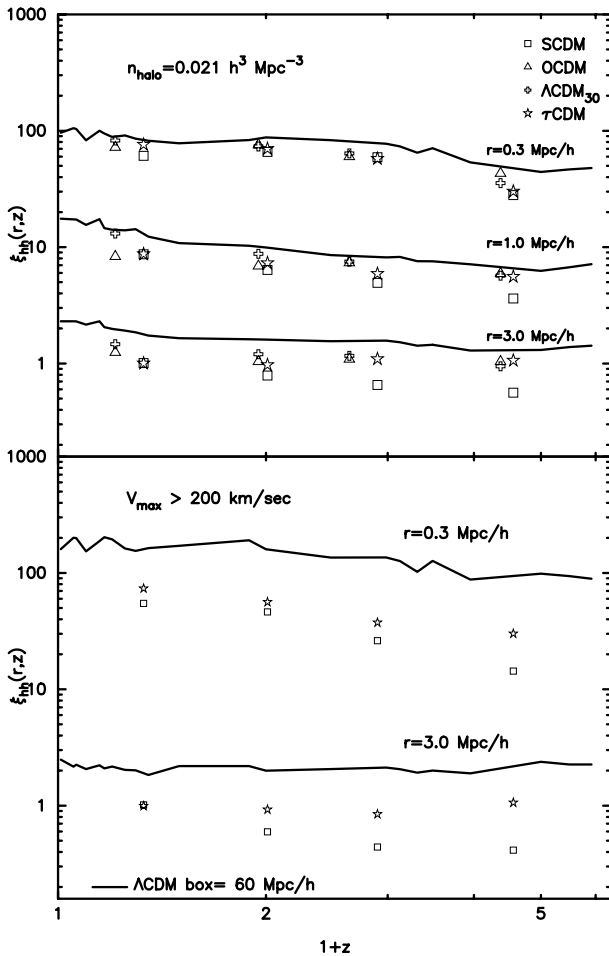


FIG. 13.—Evolution of the halo correlation function at various scales for all models. The correlation functions shown in the upper panel were computed using a fixed number density of halos (implying different limits on the maximum circular velocity cut). The correlation functions shown in the lower panel were computed using all halos with V_{\max} larger than 200 km s^{-1} . Results for only two $30 h^{-1} \text{ Mpc}$ simulations are presented in this panel. The other two simulations had too small a number of halos. The solid lines in both panels represent results for the ΛCDM model with the ART code in the $60 h^{-1} \text{ Mpc}$ box.

combine high-resolution dissipationless simulations with semianalytical models of galaxy formation (e.g., Kauffmann et al. 1998) are also in good agreement with the results of this paper.

Although our definition of a halo is different from that used in the conventional Press-Schechter framework, we believe that it is closer to what can be identified in a simulation as a galaxy location. It seems likely that in every sufficiently massive ($M \gtrsim 10^{11} h^{-1} M_{\odot}$) gravitationally bound halo baryons will cool, form stars, and produce an object resembling a galaxy (e.g., Kauffmann, Nusser, & Steinmetz 1997; Roukema et al. 1997; Yepes et al. 1997; Salucci & Persic 1997). We believe, therefore, that each of the halos in our catalog can be associated with a “galaxy.” Observationally, many distinct galaxies are located well inside the virial radii of massive galaxies, groups, and clusters. These galaxies, nonexistent by definition in the “virial overdensity” halo catalogs, are included in galaxy surveys and are used to compute the correlation function. Our definition, therefore, is natural, if the goal is to compare the observations with predictions of the numerical simulations.

Although, as we discussed above (§ 4.3), the resolution (and, correspondingly, the computational costs) required for galaxy-size halos to survive in the tidal fields of high-density regions is quite high, the subsequent comparison with the observations is straightforward and does not require ambiguous corrections for the “overmerging.”

In the dissipationless simulations reported in this paper, we cannot unambiguously assign type, color, luminosity, or other galactic properties to our halos without additional modeling. Our results, therefore, should be applicable to “global” galaxy surveys, such as the APM survey, in which galaxies are selected solely on the basis of their luminosity (related to halo mass via the Tully-Fisher or Faber-Jackson relation). Nevertheless, without detailed knowledge of galaxy properties we can model the observational selection effects only approximately. For example, some of the DM halos may harbor low surface brightness galaxies which could be missing in galaxy catalogs, while the luminosity of some smaller mass halos may be affected by processes of supernovae-driven winds, photoionization, etc. Inclusion of such processes is required for accurate comparisons with observations. The agreement between the correlation functions of halos in our ΛCDM simulations and the APM galaxies may thus indicate that the effects of the above processes are not strong and our halo catalogs are representative of the overall galaxy population and therefore success of the ΛCDM model. On the other hand, if the additional physics is important and has a great effect on the predicted correlation function, the agreement indicates that this model fails to explain the galaxy clustering.

In § 5.2 we have compared the correlation function of halos ξ_{hh} in our $60 h^{-1} \text{ Mpc}$ ΛCDM simulation with the $z = 0$ correlation function of galaxies ξ_{gg} (Baugh 1996) in the APM catalog (Loveday et al. 1995) and have found a very good agreement between the two. The APM galaxy correlation function is measured very accurately, which makes the agreement within the 1σ error bars very striking (see Fig. 7). Recently, the advent of new faint galaxy surveys allowed the measurement of the clustering surveys at redshifts of $z \approx 0-1$ (e.g., Le Fèvre et al. 1996; Shepherd et al. 1997; Carlberg et al. 1997; Connolly, Szalay, & Brunner 1998; Postman et al. 1998; Carlberg et al. 1998). Unfortunately, there is some disagreement between these studies concerning the amplitude of the clustering signal, which possibly indicates that there is morphology and/or luminosity segregation in the clustering of the intermediate-redshift galaxies. It is indeed true that the correlation amplitude depends on the luminosity of the galaxies (e.g., Carlberg et al. 1998; Postman et al. 1998). The comoving correlation length r_0 measured in these surveys varies, generally lying in the range $r_0 \sim 2-4 h^{-1} \text{ Mpc}$ with an average value of about $r_0 \approx 3 h^{-1} \text{ Mpc}$. The correlation length of bright galaxies is, however, somewhat larger and consistent with the correlation length of the local galaxies $r_0 \approx 5 h^{-1} \text{ Mpc}$ (Carlberg et al. 1998; Postman et al. 1998). Comparison of the above values of r_0 with correlations in our ΛCDM simulation (Table 4) shows that we predict a correlation length in good agreement with that of bright galaxies and somewhat larger than the r_0 -value of the faint galaxies. The latter, however, is measured with rather large uncertainties, and our values of r_0 are actually consistent with the observed ones within 1σ .

Remarkable progress of the high-redshift galaxy detection techniques, based on the search for the signatures of the

Lyman break in the colors of faint galaxies (Steidel & Hamilton 1992, 1993), resulted in a rapid growth of the amount and quality of the clustering observations at $z \approx 3$ (Steidel et al. 1998; Giavalisco et al. 1998; Adelberger et al. 1998). These ‘‘Lyman-break galaxies’’ (LBGs) were found to be clustered at $z \approx 3$ as strongly as the present-day galaxies. The real space correlation function of these galaxies was well described by the conventional power-law form with the value of the slope γ and the correlation length r_0 consistent with the $z \approx 0$ values (Giavalisco et al. 1998): $\gamma \approx 1.7\text{--}2.2$ and $r_0 \approx 3 h^{-1}$ Mpc. These values are in reasonably good agreement with $z = 3$ values for our $V_{\max} > 120$ km s $^{-1}$ catalog (Table 4). The value of bias that is measured for the LBGs at scales of $\approx 5\text{--}10 h^{-1}$ Mpc is $b \sim 1.5, 3.6, 4.5$, for the $\Omega_0 = 1$, $\Omega_0 = 0.2$ (open), and $\Omega_0 = 0.3$ (flat) models, respectively (Giavalisco et al. 1998; Adelberger et al. 1998). These values can be compared with $b(z = 3)$ for halos in our simulations, shown in Figures 8 and 14. All models agree with the observations, within the uncertainties of the galaxy-to-halo mapping. This result is in general agreement with the results of the numerous recent numerical studies that modeled the clustering of LBGs (e.g., Wechsler et al. 1998; Jing & Suto 1998; Bagla 1998; Governato et al. 1998). However, there appear to be some puzzling details in comparisons with the data. The observed value of $b_{\text{LBG}} \approx 3\text{--}4$

can be reproduced in the Λ CDM for massive halos with $V_{\max} > 200$ km s $^{-1}$ (Fig. 8, *top panel*). This is in agreement with almost all other theoretical studies. However, the correlation function of the LBGs measured by Giavalisco et al. (1998) does not agree with the correlation function measured for the $V_{\max} > 200$ km s $^{-1}$ of our Λ CDM halos: $r_0 \approx 3 h^{-1}$ Mpc for LBGs versus $r_0 \approx 4.5 h^{-1}$ Mpc for the halos. This disagreement was actually noticed in the study of Adelberger et al. (1998), who used the count-in-cells analysis to derive the value of bias. The values of the parameters of the correlation function that were derived from the observed rms fluctuations of galaxies in cells of $\approx 12 h^{-1}$ Mpc ($\sigma_{\text{gal}} \approx 1.1 \pm 0.2$) are considerably higher than those measured directly by Giavalisco et al. (1998). The corresponding value of $\sigma_{\text{halo}}(r = 12 h^{-1}$ Mpc) in our Λ CDM simulation is $\approx 0.6, 0.7, 0.9$ for halos with $V_{\max} > 120, 150, 200$ km s $^{-1}$, respectively. This is consistent with the interpretation of the LBGs as objects residing inside massive ($V_{\max} > 200$ km s $^{-1}$ or $M \gtrsim 10^{12} h^{-1} M_{\odot}$) DM halos. This result supports the interpretation of Adelberger et al. (1998) and suggests that the correlation amplitude of the LBGs may be higher than that obtained from the observed angular correlation function (Giavalisco et al. 1998).

Overall, we believe that the comparisons discussed above indicate that there is good agreement between our results and the clustering data at both low and high redshifts. This implies that hierarchical models in which observed galaxies form in the host DM halos naturally explain the observed galaxy clustering at different epochs, including excellent agreement with the accurately measured $z = 0$ correlation function. On the other hand, the generic form of the bias evolution observed in the numerical simulations at high redshifts agrees well with the prediction of the analytical models based on the extended Press-Schechter formalism. This implies that we understand the nature of the bias and the processes that drive its evolution at high z . At low redshifts, the bias evolution of gravitationally bound halos is driven by the dynamical processes inside the nonlinear structures which are largely independent of cosmology. The study of these processes is important for a successful modeling of galaxy clustering at $z \lesssim 1$.

7. SUMMARY

We have studied the evolution of the correlation function and bias of galaxy-size halos in different cosmological models (Λ CDM, OCDM, τ CDM, and SCDM). The high resolution of our numerical simulations allowed us to avoid the overmerging in the high-density regions and estimate the correlation amplitude and bias directly at small (down to $\sim 100 h^{-1}$ kpc) scales. The main results and conclusions presented in this paper are as follows:

1. At all epochs, the two-point correlation function of galaxy-size halos ξ_{hh} is well approximated by a power law $\xi_{\text{hh}} = (r/r_0)^{-\gamma}$ with the slope $\gamma \approx 1.6\text{--}1.8$. The correlation length r_0 at $z = 0$ is $\approx 5 h^{-1}$ Mpc, regardless of the minimal mass limit of the halo samples. At high redshifts, the correlation function evolves nonmonotonically: r_0 decreases somewhat between redshifts of 5 and 3 and then increases steadily until $z = 0$. For the most massive halos, the correlation length at $z \approx 5$ is comparable to that at $z = 0$.

2. The difference between the shape of the ξ_{hh} and the shape of the correlation function of matter results in a scale-dependent bias at scales $\lesssim 7 h^{-1}$ Mpc. We find this to be a

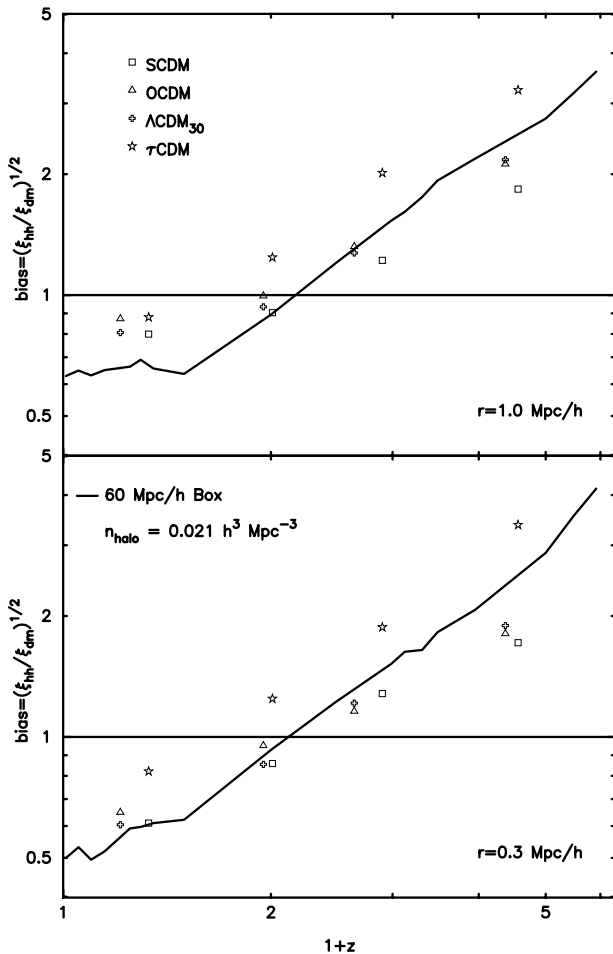


FIG. 14.—Evolution of bias for different models at two scales, $r = 1.0 h^{-1}$ Mpc (*upper panel*) and $r = 0.3 h^{-1}$ Mpc (*lower panel*). The markers show results with the AP³M code, and the solid curves represent results for the Λ CDM model with the ART code in the $60 h^{-1}$ Mpc box.

generic prediction of the hierarchical models independent of the epoch and of the model details.

3. Another generic prediction is that the comoving amplitude of the correlation function for halos above a certain mass evolves nonmonotonically: it decreases from an initially high value at $z \sim 3-7$ and very slowly increases at $z \lesssim 1$. This behavior at large scales was demonstrated by a number of authors (see § 6). Here we have shown that this behavior also applies to the correlation amplitude at small scales ($\lesssim 1 h^{-1}$ Mpc). The nonmonotonic evolution of the correlation function calls into question the usefulness of the simplistic “ ϵ -models” as a description of the clustering evolution. We note, however, that at $z \lesssim 1$ the evolution of the halo correlation function is approximately monotonic (albeit dependent on scale). The very slow evolution of the halo correlation amplitude in comoving coordinates at these redshifts implies a value of $\epsilon \approx -1$, which is in agreement with the values preferred by the observations (e.g., Postman et al. 1998).

4. The evolution of the halo correlation function is very mild compared with the evolution of the DM correlation function. The latter evolves by a factor of $\sim 10-60$ (depending on scale) between redshifts of ≈ 7 and 0, while the difference in amplitude of the former between any two epochs is less than a factor of 2. The large difference in the evolution rates of the matter and halo correlation functions means that the bias evolves rapidly with cosmic time: it changes from high- b values of $\sim 2-5$ at $z \sim 3-7$ to antibias b -values of $\sim 0.5-1$ on small $\lesssim 5 h^{-1}$ Mpc scales at $z = 0$.

5. We find that our results agree well with existing clustering data at different redshifts, indicating general success of the hierarchical models of structure formation in which galaxies form inside the host DM halos. Particularly, we find excellent agreement in both slope and amplitude between $\zeta_{\text{hh}}(z=0)$ in our ΛCDM_{60} simulation and the galaxy correlation function measured using the APM galaxy survey. At high redshifts, all models reproduce well the observed clustering of the LBGs. Our results imply that for high-redshift clustering to be used as a cosmological test, it is crucial that we know what type of objects are used to estimate the clustering signal. The knowledge of the number density of objects is not sufficient (see § 5).

6. We find good agreement at $z \gtrsim 2$ between our results and predictions of the analytical models of bias evolution (MW; Matarrese et al. 1997). This indicates that we now have a solid understanding of the nature of the bias and of the processes that drive its evolution at these z . We argue,

however, that at lower redshifts the evolution of bias is driven by dynamical processes, i.e., dynamical friction and tidal stripping, inside the nonlinear high-density regions such as galaxy clusters and groups. These processes do not depend on cosmology and tend to erase the differences in clustering properties of halos that exist between cosmological models at high z . The latter result implies that low-redshift clustering is probably not a very strong discriminator between cosmological models.

We believe that the success of the current theoretical models in interpreting the clustering data forms a solid foundation for further sophistication of the models by including the processes important for galaxy formation (such as dynamics of baryons, cooling, star formation, and stellar feedback). These models would allow one to predict the observed properties of galaxies and thus mimic the observational selection criteria, allowing for a robust comparison between the model and the data. We believe that the differences between high- z clustering properties of objects in different cosmological models demonstrated in this study (see § 5), the improved theoretical models, and the ever-increasing amount of new clustering data can be successfully combined in the near future to put useful constraints on the cosmological parameters describing our universe.

This work was funded by NSF grant AST 93-19970, NASA grant NAG 5-3842, and NATO grant CRG 972148 to the NMSU. P. C. was partially supported by DGAPA/UNAM through project IN-109896. We are grateful to Stefan Gottlöber for the help in computing the correlation function of isolated halos, to Carlton Baugh for sending us the APM correlation function in electronic form, and to Adrian Jenkins for providing the Virgo dark matter correlation function in electronic form. We thank Elizabeth Rizza for the help in improving the language of the manuscript. Our ART simulations were done at the National Center for Supercomputing Applications (Urbana-Champaign, Illinois) and on the Origin-2000 computer at the Naval Research Laboratory. The AP³M simulations have been carried out on the Origin-2000 at the Dirección General de Servicios de Cómputo, UNAM, Mexico, and at the DEC Alpha Stations at CITA (Toronto, Canada). P. C. is very grateful to R. Carlberg for access to the CITA computing resources, where part of the AP³M simulations were run.

REFERENCES

- Adelberger, K. L., Steidel, C. C., Giavalisco, M., Dickinson, M., Pettini, M., & Kellogg, M. 1998, *ApJ*, 505, 18
 Bagla, J. S. 1998, *MNRAS*, 299, 417
 Bardeen, J. M. 1986, in *Inner Space/Outer Space*, ed. E. W. Kolb et al. (Chicago: Univ. Chicago Press), 212
 Bardeen, J. M., Bond, J. R., Kaiser, N., & Szalay, A. S. 1986, *ApJ*, 304, 15 (BBKS)
 Baugh, C. M. 1996, *MNRAS*, 280, 267
 Binney, J., & Tremain, S. 1987, *Galactic Dynamics* (Princeton: Princeton Univ. Press)
 Blanton, M., Cen, R., Ostriker, J. P., & Strauss, M. A. 1999, *ApJ*, 522, 590
 Bond, J. R., Cole, S., Efstathiou, G., & Kaiser, N. 1991, *ApJ*, 379, 440
 Bower, R. J. 1991, *MNRAS*, 248, 332
 Brainerd, T. G., & Villumsen, J. V. 1994, *ApJ*, 431, 477
 Bunn, E. F., & White, M. 1997, *ApJ*, 480, 6
 Carlberg, R. G. 1990, *ApJ*, 359, L1
 Carlberg, R. G., Cowie, L. L., Songaila, A., & Hu, E. M. 1997, *ApJ*, 484, 538
 Carlberg, R. G., et al. 1998, in *Proc. Royal Society Discussion Meeting, Large Scale Structure in the Universe*, preprint (astro-ph/9805131)
 Catelan, P., Lucchin, F., Matarrese, S., & Porciani, C. 1998a, *MNRAS*, 297, 692
 Catelan, P., Matarrese, S., & Porciani, C. 1998b, *ApJ*, 502, L1
 Cen, R., Gnedin, N. Y., & Ostriker, J. P. 1992, *ApJ*, 417, 387
 Cen, R., & Ostriker, J. P. 1992, *ApJ*, 399, L113
 ———. 1998, *ApJ*, submitted (astro-ph/9809370)
 Chaboyer, B. 1998, *Phys. Rep.*, in press
 Cole, S., & Kaiser, N. 1989, *MNRAS*, 237, 1127
 Cole, S., Weinberg, D. H., Frenk, C. S., & Ratra, B. 1997, *MNRAS*, 289, 37
 Coles, P. 1993, *MNRAS*, 262, 1065
 Colin, P., Carlberg, R. G., & Couchman, H. M. P. 1997, *ApJ*, 490, 1
 Connolly, A. J., Szalay, A. S., & Brunner, R. J. 1998, *ApJ*, 499, L125
 Couchman, H. M. P. 1991, *ApJ*, 368, L23
 Davis, M., Efstathiou, G., Frenk, C. S., & White, S. D. M. 1985, *ApJ*, 292, 371
 Dekel, A., & Lahav, O. 1999, *ApJ*, 520, 24
 Dekel, A., & Rees, M. J. 1987, *Nature*, 326, 455
 Dekel, A., & Silk, J. 1986, *ApJ*, 303, 39
 Dubinski, J. 1998, *ApJ*, 502, 141

- Efstathiou, G., Bond, J. R., & White, S. D. M. 1992, *MNRAS*, 258, 1P
 Efstathiou, G., Davis, M., Frenk, C. S., & White, S. D. M. 1985, *ApJS*, 57, 241
 Eke, V. R., Cole, S., & Frenk, C. S. 1996, *MNRAS*, 282, 263
 Eke, V. R., Cole, S., Frenk, C. S., & Henry, P. J. 1998, *MNRAS*, 298, 1145
 Evrard, A. E. 1997, *MNRAS*, 292, 289
 Falco E. E., Shapiro, I. I., Moustakas, L. A., & Davis, M. 1997, *ApJ*, 484, 70
 Frenk, C. S., White, S. D. M., Davis, M., & Efstathiou, G. 1988, *ApJ*, 327, 507
 Fry, J. N. 1996, *ApJ*, 461, L65
 Ghigna, S., Moore, B., Governato, F., Lake, G., Quinn, T., & Stadel, J. 1998, *MNRAS*, 300, 146
 Giavalisco, M., Steidel, C. C., Adelberger, K. L., Dickinson, M. E., Pettini, M., & Kellogg, M. 1998, *ApJ*, 503, 543
 Governato, F., Baugh, C. M., Frenk, C. S., Cole, S., Lacey, C. G., Quinn, T., & Stadel, J. 1998, *Nature*, 392, 359
 Hamilton, A. J. S., Kumar, P., Lu, E., & Mathews, A. 1991, *ApJ*, 374, L1
 Hockney, R. W., & Eastwood, J. W. 1981, *Computer Simulations Using Particles* (New York: McGraw-Hill)
 Jain, B., Mo, H. J., & White, S. D. M. 1995, *MNRAS*, 276, L25
 Jenkins, A., et al. (The Virgo Consortium). 1998, *ApJ*, 499, 20
 ———. 1999, in preparation (presented as a poster at the Conference Evolution of Large-Scale Structure: From Recombination to Garching (Garching, 1998 August))
 Jing, Y. P. 1998, *ApJ*, 503, L9
 Jing, Y. P., & Suto, Y. 1998, *ApJ*, 494, L5
 Kaiser, N. 1984, *ApJ*, 284, L9
 Kaiser, J. M. 1986, in *Inner Space/Outer Space*, ed. E. W. Kolb et al. (Chicago: Univ. Chicago Press), 258
 Katz, N., Hernquist, L., & Weinberg, D. H. 1999, *ApJ*, 523, 463
 Kauffman, G., Colberg, J. M., Diaferio, A., & White, S. D. M. 1999, *MNRAS*, 303, 188
 Kauffmann, G., Nusser, A., & Steinmetz, M. 1997, *MNRAS*, 286, 795
 Kauffmann, G., White, S. D. M., & Guiderdoni, B. 1993, *MNRAS*, 264, 201
 Kim, A. G., et al. 1997, *ApJ*, 476, L63
 Kitayama, T., & Suto, Y. 1996, *ApJ*, 469, 480
 Klypin, A. A., Gottlöber, S., Kravtsov, A. V., & Khokhlov, A. M. 1999, *ApJ*, 516, 530 (KGKK)
 Klypin, A. A., & Holtzman, J. 1997, preprint (astro-ph/9712217)
 Klypin, A. A., Nolthenius, R., & Primack, J. 1997, *ApJ*, 474, 533
 Klypin, A. A., Primack, J., & Holtzman, J. 1996, *ApJ*, 466, 13
 Kravtsov, A. V., & Klypin, A. A. 1999, *ApJ*, 520, 437
 Kravtsov, A. V., Klypin, A. A., Bullock, J. S., & Primack, J. R. 1998, *ApJ*, 502, 48
 Kravtsov, A. V., Klypin, A. A., & Khokhlov, A. M. 1997, *ApJS*, 111, 73
 Lacey, C., & Cole, S. 1994, *MNRAS*, 271, 676
 Le Fèvre, O., Hudon, D., Lilly, S. J., Crampton, D., Hammer, F., & Tresse, L. 1996, *ApJ*, 461, 534
 Loveday, J., Maddox, S. J., Efstathiou, G., & Peterson, B. A. 1995, *ApJ*, 442, 457
 Maddox, S. J., Efstathiou, G., & Sutherland, W. J. 1996, *MNRAS*, 283, 1227
 Mann, R. G., Peacock, J. A., & Heavens, A. F. 1998, *MNRAS*, 293, 209
 Matarrese, S., Coles, P., Lucchin, F., & Moscardini, L. 1997, *MNRAS*, 286, 115
 Mo, H. J., Jing, Y. P., & White, S. D. M. 1996, *MNRAS*, 282, 1096
 Mo, H. J., Mao, S., & White, S. D. M. 1998, *MNRAS*, 295, 319
 Mo, H. J., & White, S. D. M. 1996, *MNRAS*, 282, 347 (MW)
 Moore, B., Katz, N., & Lake, G. 1996, *ApJ*, 457, 455
 Moscardini, L., Coles, P., Lucchin, F., & Matarrese, S. 1998, *MNRAS*, 299, 95
 Navarro, J., Frenk, C., & White, S. D. M. 1996, *ApJ*, 462, 563 (NFW)
 Nolthenius, R., Klypin, A., & Primack, J. R. 1997, *ApJ*, 480, 43
 Nusser, A., & Davis, M. 1994, *ApJ*, 421, L1
 Peacock, J. A., & Dodds, S. J. 1994, *MNRAS*, 267, 1020
 ———. 1996, *MNRAS*, 280, L19
 Postman, M., Lauer, T. R., Szapudi, I., & Oegerle, W. 1998, *ApJ*, 506, 33
 Press, W. H., & Schechter, P. 1974, *ApJ*, 187, 425
 Press, W. H., Teukolsky, S. A., Vetterling, W. T., & Flannery, B. P. 1992, *Numerical Recipes* (2d ed.: Cambridge: Cambridge Univ. Press)
 Rees, M. J. 1985, *MNRAS*, 213, 75P
 Roukema, B. F., Peterson, B. A., Quinn, P. J., & Rocca-Volmerange, B. 1997, *MNRAS*, 292, 835
 Salaris, M., & Cassisi, S. 1998, *MNRAS*, 298, 166
 Salucci, P., & Persic, M. 1997, in *ASP Conf. Ser. 117, Dark and Visible Matter in Galaxies*, ed. M. Persic & P. Salucci (San Francisco: ASP), 1
 Schaeffer, R., & Silk, J. 1985, *ApJ*, 292, 319
 Shepherd, C. W., Carlberg, R. G., Yee, H. K. C., & Ellingson, E. 1997, *ApJ*, 479, 82
 Silk, J. 1985, *ApJ*, 297, 1
 Smith, C. C., Klypin, A. A., Gross, M. A. K., Primack, J. R., & Holtzman, J. 1998, *MNRAS*, 297, 910
 Steidel, C. C., Adelberger, K. L., Dickinson, M., Giavalisco, M., Pettini, M., & Kellogg, M. 1998, *ApJ*, 492, 428
 Steidel, C. C., & Hamilton, D. 1992, *AJ*, 104, 941
 ———. 1993, *AJ*, 105, 2017
 Sugiyama, N. 1995, *ApJS*, 100, 281
 Summers, F. J., Davis, M., & Evrard, A. E. 1995, *ApJ*, 454, 1
 Tegmark, M., & Peebles, P. J. E. 1998, *ApJ*, 500, L79
 Walker, T. P., Steigman, G., Schramm, D. N., Olive, K. A., & Kang, H.-S. 1991, *ApJ*, 376, 51
 Wechsler, R. H., Gross, M. A. K., Primack, J. R., Blumenthal, G. R., & Dekel, A. 1998, *ApJ*, 506, 19
 Yepes, G., Kates, R., Khokhlov, A., & Klypin, A. 1997, *MNRAS*, 284, 235